Published in final edited form as:
Inorg Chem. 2009 April 6; 48(7): 2735–2747. doi:10.1021/ic802192w.

Mössbauer, Electron Paramagnetic Resonance, and Theoretical Study of a Carbene-based All-ferrous Fe_4S_4 Cluster: Electronic Origin and Structural Identification of the Unique Spectroscopic Site

Mrinmoy Chakrabarti[a], **Liang Deng**[b], **R. H. Holm**[b,*], **Eckard Münck**[a,*], and **Emile L. Bominaar**[a,*]

[a] Department of Chemistry, Carnegie Mellon University, Pittsburgh, PA 15213

[b] Department of Chemistry and Chemical Biology, Harvard University, Cambridge, MA 02138

Abstract

It is well established that the cysteinate-coordinated $[Fe_4S_4]$ cluster of the Fe-protein of nitrogenase from *A. vinelandii* (*Av*2) can attain the all-ferrous core oxidation state. Mössbauer and EPR studies have shown that the all-ferrous cluster has a ground state spin $S = 4$ and an effective 3:1 site symmetry in the spin structure and ^{57}Fe quadrupole interactions. Recently Deng and Holm reported the synthesis of $[Fe_4S_4(Pr^i_2NHCMe_2)_4]$,[2] **1**, ($Pr^i_2NHCMe_2$ = 1,3-diisopropyl-4,5-dimethylimidazol-2-ylidene) and showed that the all-ferrous carbene-coordinated cluster is amenable to physico–chemical studies. Mössbauer and EPR studies of **1**, reported here, reveal that the electronic structure of this complex is strikingly similar to that of the protein-bound cluster, suggesting that the ground state spin and the 3:1 site ratio are consequences of spontaneous distortions of the cluster core. To gain insight into the origin of the peculiar ground state of the all-ferrous clusters in **1** and *Av*2, we have studied a theoretical model that is based on a Heisenberg–Dirac–Van Vleck Hamiltonian whose exchange-coupling constants are a function of the Fe–Fe distances. By combining the exchange energies with the elastic deformation energies in the harmonic approximation, we obtain for a T_2 distortion a minimum with spin $S = 4$ and a C_{3v} core structure in which one iron is unique and three irons are equivalent. This minimum has all the spectroscopic and structural characteristics of the all-ferrous clusters of **1** and *Av*2. Our analysis maps the unique spectroscopic iron site to a specific site in the X-ray structure of the $[4Fe\text{-}4S]^0$ core both in complex **1** and in *Av*2.

1. Introduction

The recent syntheses and structural determinations of $[Fe_4S_4(CN)_4]^{4-}$ 1 and the carbene-ligated cluster $[Fe_4S_4(Pr^i_2NHCMe_2)_4]$,[2] **1**, complete the set of accessible cubane-type clusters having core oxidation levels $[Fe_4S_4]^z$ with charge z ranging from 0 to 3+.[3] The cluster with $z = 0$ is of particular current interest because its all-ferrous core is isoelectronic with that present in the iron protein of *A. vinelandii* nitrogenase (called Fe-protein or *Av*2) when reduced with Ti(III) citrate.[4-6] Furthermore, the synthetic cluster cores are nearly isostructural with the $[Fe_4S_4]^0$ core of the fully reduced $[Fe_4S_4(S_{Cys})_4]$ cluster of the iron protein.[2,7] The carbene cluster, whose structure is depicted in Figure 1, is far more amenable to experimentation than the cyanide cluster because of its lesser tendency toward oxidation. The compound crystallizes in the monoclinic space group *Cc*; the cluster has the familiar cubane-type stereochemistry with

E-mail: ELB: eb7g@andrew.cmu.edu, EM: emunck@cmu.edu, RHH: holm@chemistry.harvard.edu.

no imposed symmetry and Fe–S bond lengths and other structural features consistent with the all-ferrous formulation.[2]

For the all-ferrous $[Fe_4S_4]^0$ cluster of *Av*2 a parallel mode EPR and Mössbauer spectroscopic study of the fully reduced native cluster demonstrated an effective 3:1 symmetry of iron sites that afford an $S = 4$ cluster ground state, rather than an $S = 0$ state as expected for a symmetric cubane core.[6] This state is unique amongst protein-bound metal sites of any nuclearity, and thus raises the issue of the effect of protein structure and environment on stabilizing this state. The cluster is bound between two identical subunits of the Fe-protein and is potentially susceptible to the influence of both protein structure and solvent. Further attention is directed toward native cluster properties by the report of an $[Fe_4S_4]^0$ cluster with a probable $S = 4$ state in the activator protein of a dehydratase,[8] and the claim of an $S = 0$ all-ferrous cluster in the *A. vinelandii* Fe-protein when reduced with flavodoxin hydroquinone.[9] A detailed EPR and Mössbauer analysis of the carbene cluster, presented here, revealed that **1** has an $S = 4$ ground state like the *Av*2 $[Fe_4S_4]^0$ cluster. Moreover, the analysis indicates striking similarities between the ^{57}Fe hyperfine parameters. Given that the two clusters have different external coordination, these findings suggested to us that the $S = 4$ ground state and the observed 3:1 site ratios reflect intrinsic properties of the cluster core rather than a perturbing influence of the environment. For small variations, the Fe–Fe distances, $\Delta r_{i,j}$, are linearly related to changes of the exchange-coupling constants, $\Delta J_{i,j}$. Using this correlation we have investigated the energy surfaces of the combined actions of elastic and exchange forces, finding that a global minimum is attained for a T_2 mode acting in the $S = 4$ manifold that yields a 3:1 pattern of magnetic hyperfine interactions, as observed experimentally.

Elsewhere we have provided a perspective of the carbene cluster in relation to the protein-bound all-ferrous cluster.[10]

2. Materials and Methods

$[Fe_4S_4(Pr^i_2NHCMe_2)_4]$, **1**, was prepared as described.[2] To avoid orientation of the polycrystalline material in the Mössbauer spectrometer by the applied magnetic field, the sample was stirred into 0.3 mL Paraton-N oil before freezing. For EPR studies solid **1** was dissolved in toluene to yield a 7.9 mM solution.

Mössbauer spectra were collected with constant acceleration spectrometers, using two cryostats that allowed studies at 4.2 K in applied fields up to 8.0 T. Isomer shifts are quoted relative to Fe metal at 298 K. Spectra were analyzed with the WMOSS software package (WEB Research Co., Edina, MN). X-band EPR spectra were recorded at on a Bruker EMX spectrometer, using a Hewlett-Packard 5352B microwave frequency counter, the ER4102 ST cavity, and the Oxford Instruments ESR 900 Cryostat. Spectra were analyzed with the program SpinCount written by M. P. Hendrich at Carnegie Mellon University.

3. Results

3.1. Mössbauer studies of polycrystalline 1

We have studied a polycrystalline sample of all-ferrous **1** with Mössbauer spectroscopy between 2 K and 140 K in applied magnetic fields up to 8.0 T. An EPR study of the polycrystalline material was unsuccessful, for two reasons. First, the observed resonances were very broad and, second, at low temperatures the uniaxial electronic system led to partial alignment of crystallites by the applied field. We therefore decided to study the EPR spectra of **1** in toluene, a glassing solvent that produced well resolved spectra. We discuss the Mössbauer spectra first, using from EPR the information that 1 has an $S = 4$ ground state with zero-field splitting (ZFS) parameters $D = -1.9$ cm^{-1} and $E/D \approx 0.07$. Figure 2 shows a series

of 4.2 K spectra, recorded in applied field as indicated, and Figure 3 features a zero field and an 8.0 T spectrum, both recorded at 100 K.

The Mössbauer and EPR spectra were analyzed with the $S = 4$ spin Hamiltonian

$$\widehat{\mathcal{H}} = \widehat{\mathcal{H}}_{\mathrm{e}} + \widehat{\mathcal{H}}_{\mathrm{hf}} \tag{1}$$

$$\widehat{\mathcal{H}}_{\mathrm{e}} = D\left[\widehat{\mathrm{S}}_{\mathrm{z}}^2 - 20/3 + (E/D)\left(\widehat{\mathrm{S}}_{\mathrm{x}}^2 - \widehat{\mathrm{S}}_{\mathrm{y}}^2\right)\right] + \beta \widehat{\mathrm{S}} \cdot \mathrm{g} \cdot \mathrm{B} \tag{2}$$

$$\widehat{\mathcal{H}}_{\mathrm{hf}} = \sum\nolimits_{\mathrm{i}=1,4} \left\{\widehat{\mathrm{S}}_{\mathrm{i}} \cdot \mathrm{A}_{\mathrm{i}} \cdot \widehat{\mathrm{I}}_{\mathrm{i}} - g_{\mathrm{n}}\beta_{\mathrm{n}}\mathrm{B} \cdot \widehat{\mathrm{I}}_{\mathrm{i}} + \widehat{\mathcal{H}}_{\mathrm{Q,i}}\right\} \tag{3}$$

$$\widehat{\mathcal{H}}_{\mathrm{Q,i}} = \frac{1}{12} eQV_{\mathrm{i},\zeta\zeta} \left[3\widehat{\mathrm{I}}_{\mathrm{i},\zeta}^2 - \mathrm{I}(\mathrm{I}+1) + \eta_{\mathrm{i}}\left(\widehat{\mathrm{I}}_{\mathrm{i},\xi}^2 - \widehat{\mathrm{I}}_{\mathrm{i},\eta}^2\right)\right] \tag{4}$$

where all the parameters have their conventional meaning. In eq 2 we have written the ZFS term in its principal axis system {x,y,z}, which we will use as our frame of reference. For our Mössbauer analysis we have used an isotropic g-tensor and set $g = 2$ ($g_z = 2.02$ from EPR, see below). Complex **1** has C_1 symmetry, implying that all tensors in eqs 1 - 4 may have different principal axis systems. In the following we discuss the main features of the Mössbauer spectra and indicate how the various parameters can be extracted.

The 4.2 K spectra of the four subsites of **1** exhibit simple 6-lines pattern. The intensities of the absorption lines did not depend on whether the applied 45 mT field was oriented parallel or perpendicular to the observed γ-radiation. This observation implies that the electronic ground state is magnetically uniaxial, i. e. the expectation value of the electron spin is non-zero only in one direction, implying that the axial parameter of the zero-field splitting tensor **D** is negative, $D < 0$. As shown in Fig. 4A and B, the same Mössbauer spectrum was observed for $B = 0$ and $B = 45$ mT. In general, the electronic levels of systems with integer electronic spin are singlets, unless degeneracies occur as a consequence of symmetry. In the absence of an applied magnetic field an electronic singlet does not yield a Mössbauer spectrum exhibiting magnetic hyperfine structure, in contrast to what is observed for **1**. It follows that the spin ground state of **1** must be degenerate. It was shown in [ref 11] that ^{57}Fe magnetic hyperfine structure is observed for $B = 0$ if the splitting Δ of the $M_S = \pm S$ levels (here $M_S = \pm 4$) fulfills the condition $\Delta < |A_{i;z}|$ where $A_{i;z}$ is the component of the magnetic hyperfine tensor of site i along the z-axis of the ZFS tensor. Typically, A-values of $[Fe_4S_4]$ clusters are of the order 10 MHz, implying that Δ has to be smaller than 10^{-3} cm^{-1}. For an $S = 4$ system the splitting of the $M_S = \pm 4$ doublet is given by $\Delta = 2.2\, D(E/D)^4$ and thus the condition $\Delta < 10^{-3}$ cm^{-1} may often be fulfilled for $E/D \leq 0.1$ as long as D is only a few wavenumbers.

For small D values the $M_S = \pm 4$ multiplet is readily magnetized along the z-axis, yielding for $\beta B/|D| \ll 1$ a large disparity in the components of the spin expectation values of the ground state, $\langle S_x \rangle = \langle S_y \rangle \approx 0$ and $\langle S_z \rangle = -4$ (see Figure S1). The magnetic hyperfine field at the ^{57}Fe nucleus can be written as[12]

$$B_{int,i} = -\langle \hat{S} \rangle \cdot A_i / g_n \beta_n \quad (5)$$

For small applied fields $\mathbf{B}_{int,i}$ assumes a fixed orientation relative to the EFG tensor, described by the polar angles θ_i and φ_i. The low field spectra then depend on $\Delta E_{Q,i}$, η_i, $\mathbf{B}_{int,i}$, θ_i and φ_i. It has been shown that there exists an infinite manifold of $\{\eta_i, \theta_i, \varphi_i\}$ values that yield identical Mössbauer spectra (This so-called ambiguity problem has been described in the literature, [refs 13, 14]). In strong applied magnetic fields, where $\langle S_x \rangle$ and $\langle S_y \rangle$ compete with $\langle S_z \rangle$, and each set $\{\eta_i, \theta_i, \varphi_i\}$ may yield unique spectra. Thus, a parameter set that fits at low field may fail to do so at high field. The low temperature spectra of Figure 2 depend on as many as 50 parameters: namely D, E/D, together with four sets of $\{A_{x'}, A_{y'}, A_{z'}, \Delta E_Q, \eta, \delta, \alpha_A, \beta_A, \gamma_A, \alpha_{EFG}, \beta_{EFG}, \gamma_{EFG}\}_i$. Here $\{x', y', z'\}$ denotes the principal axis system of the A-tensor and α_A, β_A, γ_A are the Euler angles that rotate $\{x', y', z'\}$ into the principal axis system $\{x, y, z\}$ of the ZFS tensor, our system of reference; α_{EFG}, β_{EFG}, γ_{EFG} rotate the EFG tensor into $\{x, y, z\}$. All rotations are those used in WMOSS; note that WMOSS uses the "x"-convention for the Euler angles. D, E/D, ΔE_Q, and δ are reasonably well determined from considerations given below. In the following we describe how the various parameters were determined.

At 4.2 K the electronic spin of **1** relaxes slowly on the time scale of Mössbauer spectroscopy (ca. 10 MHz). As the temperature is raised above 4.2 K the absorption features broaden in a way characteristic of intermediate relaxation rates. At T = 100 K the spin system is nearly in the fast relaxation limit, and consequently quadrupole doublets are observed. Figure 3A shows a zero field spectrum recorded at 100 K. This spectrum exhibits two doublets in a 3:1 intensity ratio, similar to what has been reported for the all-ferrous *Av*2 cluster. The most noteworthy differences between the two clusters are the smaller isomer shifts of **1**, namely δ = 0.62 mm/s for sites 1-3 and δ = 0.54 mm/s for site 4 ($\Delta E_{Q,4}$ = 2.92 mm/s at 100 K). The quadrupole splittings of sites 1-3 are quite similar and not resolved, $\Delta E_Q \approx$ 1.5 - 1.6 mm/s, but distinctly smaller than that of site 4. The spectrum in Figure 3B was recorded in a parallel field of 8.0 T. Matching the splittings of the theoretical curves with the experimental data requires $B_{int,1,2,3} < 0$ and $B_{int,4} > 0$, suggesting that the local S = 2 spins of the four high-spin ferrous sites are coupled similarly as in the protein-bound cluster, namely the spins of sites 1, 2, and 3 are aligned parallel to the cluster spin and that of site 4 antiparallel.

Analysis of the spectra of Figure 2 shows that at 4.2 K only the $M_S = \pm 4$ doublet is populated; for $D = -1.9$ cm^{-1} (see below) the $M_S = \pm 3$ quasi-doublet is at energy $E/k_B \approx 19$ K. The quasi-degenerate ground state has g_{eff} = 16 and the system is essentially in the $M_S = -4$ level for $B > 1$ T. Inspection of the applied field spectra in Figure 2 shows that most absorption lines move towards the center with increasing applied fields, implying that they belong to sites with negative B_{int} while some, namely those belonging to site 4 (arrows), move outward and have $B_{int} > 0$. From the 100 K data it follows that the outward moving lines in Figure 3B belong to site 4. Outward and inward moving lines must belong to different iron sites. Figure 5 shows the 45 mT Mössbauer spectrum of Figure 4B together with the theoretical spectra of the subsites (the sum of these spectra is shown in Figure 2). We believe that this decomposition is essentially correct. In searching for a decomposition of the spectra we observed that two sites, 2 and 3, gave essentially identical spectra, and thus we have treated them henceforth as one site accounting for 50% of the spectral intensity.

We mentioned above that the parameter set obtained at low applied fields is not unique. For **1** one has to apply fields larger than 5 T to induce sizable expectation values $\langle S_x \rangle$ and $\langle S_y \rangle$. We have used the 8.0 T spectrum of Figure 2 for reducing the ambiguities of the low field spectra, using the following procedure. Starting with the parameters obtained at low field, we have least-squares fitted all spectra of Figure 2 as a group, allowing all parameters except D,

E/D, ΔE_Q, and δ to vary freely. This procedure produced a set of parameters (Table 1) that represented the set of spectra quite well. Interestingly, for this parameter set the *A*-tensors of sites 1 and 4 were found to be aligned with {x, y, z}, implying that, at low field, $\mathbf{B}_{int,1}$ and $\mathbf{B}_{int,4}$ are along the easy axis of magnetization, the z axis of eq 2. For sites 2, 3 the z′ axis of $\mathbf{A}_{2,3}$ is tilted by $\beta_A = 15$ ° relative to the z axis.

We mentioned above that, at low field, there exists an infinite manifold of $\{\eta_i, \theta_i, \varphi_i\}$ values yielding the same Mössbauer spectrum (for sites 1 and 4 the polar angles θ and φ correspond to β_{EFG} and γ_{EFG}; for sites 2, 3 they relate the EFG tensor to $\mathbf{B}_{int,2,3}$). However, the ranges of these three parameters can often be narrowed considerably. In order to explore the allowed ranges, we have used the following procedure: We have taken the simulated spectra of Figure 2 and added random noise to treat them in WMOSS as an “experimental” spectrum. We have least-squares fitted these “experimental” spectra by fixing one of the three parameters and exploring whether a good fit could be obtained. The ranges of allowed $\{\eta_i, \theta_i, \varphi_i\}$ are indicated in Table S1.

The zero-field splitting parameters *D* and *E/D* differ substantially for the all-ferrous *Av*2 cluster and the synthetic model **1**. The former has $D = -0.7$ cm^{-1} and $E/D = 0.33$ whereas **1** has $D = -1.9$ cm^{-1} and $E/D = 0.07$. The larger *D* value of **1** implies that the electronic levels are less mixed at 8.0 T, rendering the Mössbauer spectra less sensitive to components of the magnetic hyperfine tensors perpendicular to the electronic z axis. On the other hand, the spectra of the *Av*2 cluster are poorly resolved at high fields, a fact that severely limits the data analysis.

Using the parameters of Table 1 and assuming that the electronic system relaxes fast on the Mössbauer time scale, we have generated the theoretical curves of Figure 3B. Site 4 is well represented by these simulations. The simulation for sites 1-3 gives the right splitting but not quite the correct shape, probably because for these sites the spin system is only approximately near the fast fluctuation limit, a conclusion supported by the observation that the high-energy lines of doublets 1, 2 and 3 are broadened in the zero field spectrum of Figure 3A. We did not record an 8.0 T spectrum above 100 K because $\Delta E_{Q,4}$ decreased rapidly above 100 K, leading to a lack in resolution.

Finally, as the electron spin is in the slow fluctuation limit at 4.2 K, each populated electronic level will contribute its own Mössbauer spectrum. Our spectral simulations give no evidence for the presence of spectral components originating from the $M_S = \pm 3$ levels, yielding $|D| > 1.6$ cm^{-1}, consistent with the EPR data obtained in toluene, $D = -1.9$ cm^{-1}.

3.2. EPR studies

We have studied parallel-mode X-band EPR spectra of **1** dissolved in toluene between 2 K and 50 K. Two spectra are shown in Figure 6. The 8 K spectrum exhibits a resonance near $g_{eff} = 12$, which originates from an excited state, as the intensity of this feature declines upon lowering the temperature and nearly disappears at 2 K. At 2 K a sharp resonance, belonging to the ground state, is observed at $g_{eff} = 16.08$. We assign these resonances to an $S = 4$ system with $D < 0$. Thus, the $g_{eff} = 16.08$ features originates from the $M_S = \pm 4$ ground doublet whereas the $g_{eff} = 12$ feature reflects a transition between the $M_S = \pm 3$ levels. As discussed for the $S = 4$ system of the all-ferrous cluster of the nitrogenase Fe-protein,[6] the energy separation for each quasi-doublet is predicted from eq 2 to be

$$\delta E = \left[\Delta^2 + (2\beta g_{eff} B_z)^2\right]^{1/2} \quad (6)$$

where Δ is the zero-field splitting of the doublet. From the Mössbauer analysis of **1** we know that $\Delta_g = 2.2\,|D|\,(E/D)^4 < 10^{-3}$ cm^{-1} for the $M_S = \pm 4$ ground doublet, and thus $\delta E = 2\beta g_{eff} B_z$. For this quasi-doublet $g_{eff} = 2S g_z$, yielding $g_z = 2.015$ (g_z is defined in eq 2). With the Mössbauer estimate $D \approx -2$ cm^{-1}, it follows that $E/D < 0.12$.

The solid lines in Figure 6 are spectral simulations performed with SpinCount, using the parameters quoted in the caption. The line shape of the $g_{eff} \approx 12$ feature was simulated by assuming that E/D has a Gaussian distribution with $(E/D)_{avg} = 0.07$ and $\sigma_{E/D} = 0.03$. Although the spectral shape is reasonably well represented by the simulations, there are small discrepancies, indicating perhaps that the assumption of a Gaussian distribution for E/D is only approximately correct.

We have studied the $g_{eff} = 12$ resonance over a wide range of temperatures. This feature maximizes near $T = 12$ - 14 K and broadens steadily as the temperature is increased. By using the amplitude of the $g_{eff} = 12$ feature between 10 K and 25 K and fitting with variable packet linewidth (1 mT - 2 mT), we obtained $D = -1.9 \pm 0.3$ cm^{-1}. We also found that we get a good estimate for D and E/D by noting that the intensity of the $g_{eff} = 12$ resonance is proportional to $D(E/D)^6$. Thus, for $E/D = 0.07$ and $D = 1.9$ cm^{-1} we obtain a good amplitude match by assuming a concentration of 7.5 mM of **1**, which compares well with the actual concentration of 7.9 mM.

3.3. Comparison of Mössbauer spectra of complex 1 with those of all-ferrous *Av*2

There are interesting spectroscopic similarities between the Mössbauer spectra of the all-ferrous cluster of *Av*2 and the carbene-coordinated model complex (Figure 7). Both systems have a ground state with cluster spin $S = 4$. It is instructive to compare the 4.2 K Mössbauer spectra of complex **1** with the 1.5 K spectra of the protein observed in weak applied magnetic fields. Given that D is larger in **1**, we can use for this complex a higher temperarure without noticeably populating excited doublets. For this purpose we present the theoretical spectra. Not only do these represent the experimental data quite well, they can easily be manipulated to facilitate comparison of the relevant features. Thus, the lower isomer shifts of **1** compared to *Av*2, by ~0.08 mm/s, are consistent with the poorer electron donation of the terminal carbene ligands to the iron sites compared to the cysteine sulfurs. All Fe sites of the *Av*2 cluster have $\delta = 0.68$ mm/s at 4.2 K, and therefore we have set, for the sake of comparison, the isomeric shift for each iron site of **1** equal to 0.68 mm/s. There is a subtle point that should be mentioned: since $\Delta_g < 10^{-3}$ cm^{-1} for **1** and $30 \cdot 10^{-3}$ cm^{-1} for the *Av*2 cluster,[6] one needs a field of at least $B = 0.15$ T to fulfill the condition $g_{eff}\beta B \gg \Delta_g$ to obtain fully developed magnetic spectra in both the systems (Figure 7). Thus we have simulated the spectra of Figure 7 for $B = 0.15$ T.

Figure 7A shows that the spectra of sites 1, 2, and 3 are strikingly similar, the major difference being that the spectral sites 2 and 3 of the carbene model are indistinguishable whereas those of the *Av*2 cluster are slightly nonequivalent. In contrast, the spectra of site 4 exhibit quite different magnetic splittings (Figure 7B). We wondered whether the *Av*2 spectra would admit a solution with substantially different *A*-values for site 4. However, reexamination of the spectra confirmed that the assignments of Yoo et al.[6] are essentially correct. It should be noted that the principal values of $\mathbf{A}_4$ do not differ by much in the two systems; however, the tensors are differently oriented relative to the easy axis of magnetization, z.

4. Theoretical model for the all-ferrous cluster

4.1. Formulation of model

The following analysis rests on the assumption that the exchange interactions between the paramagnetic iron sites of the all-ferrous cluster are described by the Heisenberg– Dirac–Van Vleck Hamiltonian

$$\widehat{\mathscr{H}} = \sum_{i=1}^{3} \sum_{j=i+1}^{4} J_{ij} \widehat{S}_i \cdot \widehat{S}_j \tag{7}$$

where the $\hat{\mathbf{S}}_i$ are the spin operators of the high-spin ferrous iron sites of the cluster ($S_i = 2$, i = 1 – 4) and J_{ij} are the exchange-coupling constants between them. In general, including the case that the exchange-coupling constants have different values, the eigenstates of eq 7 are eigenfunctions of the square of the total spin operator, $\hat{\mathbf{S}}^2$, with $\widehat{S} = \sum_{i=1}^{4} \widehat{S}_i$. For T_d symmetry of the cluster all exchange-coupling constants are equal, $J_{ij} = J°$, and the energies for each value of the total spin are degenerate and given by (see Table 2)

$$E°(S) = J° \left\{ \frac{1}{2} S(S+1) - 12 \right\} \tag{8}$$

Exchange-coupling constants are known to be sensitive functions of structure, in particular of bridging bond angles and associated metal–metal distances, $J_{ij} = J(R_{ij})$ (θ_{ij} and R_{ij} in Figure 8).[15] Small variations in the distances, $R_{ij} = R° + \Delta R_{ij}$, yield linear changes in the exchange-coupling constants

$$J_{ij} \approx J° + \frac{dJ}{dR} \Delta R_{ij} = J° + \Delta J_{ij} \tag{9}$$

where $J(R°) = J°$ is the exchange-coupling constant for the undistorted cluster. The elastic deformation energies can be expressed as

$$E_{elastic} = K \sum_{i=1}^{3} \sum_{j=i+1}^{4} \Delta R_{ij}^2 = k \sum_{i=1}^{3} \sum_{j=i+1}^{4} \Delta J_{ij}^2 \tag{10}$$

K is a force constant for stretching the iron–iron distances. These distances stand in linear relation with the variations in the exchange-coupling constant (eq 9), allowing us to express the elastic energy as in the third term of eq 10, using the pseudo force constant k.

$$k = \left(\frac{dJ}{dR} \right)^{-2} K \tag{11}$$

Combining the exchange and elastic energies yields the Hamiltonian

$$\widehat{\mathscr{H}} = \sum_{i=1}^{3} \sum_{j=i+1}^{4} \left\{ \left(J° + \Delta J_{ij} \right) \widehat{S}_i \cdot \widehat{S}_j + k \Delta J_{ij}^2 \right\} \tag{12a}$$

By introducing the dimensionless parameters $\delta J_{ij} = \Delta J_{ij}/J^\circ$ and $\kappa = J^\circ k$, eq 12a can also be written as

$$\widehat{\mathscr{H}} = J^\circ \sum_{i=1}^{3} \sum_{j=i+1}^{4} \left\{ \left(1+\delta J_{ij}\right) \widehat{S}_i \cdot \widehat{S}_j + \kappa \delta J_{ij}^2 \right\} \tag{12b}$$

The space spanned by the six variables δJ_{ij} can be decomposed into irreducible representations of the T_d group, A_1 $\{a_1\}$ + E $\{e_\varepsilon, e_\theta\}$ + T_2 $\{t_1, t_2, t_3\}$. The basis vectors (in curly brackets) are given by the combinations

$$a_1 = [\delta J_{12} + \delta J_{34} + \delta J_{13} + \delta J_{24} + \delta J_{14} + \delta J_{23}]/\sqrt{6} \tag{13}$$

$$e_\varepsilon = [\delta J_{13} + \delta J_{24} - (\delta J_{14} + \delta J_{23})]/2 \tag{14a}$$

$$e_\theta = [2(\delta J_{12} + \delta J_{34}) - (\delta J_{13} + \delta J_{24} + \delta J_{14} + \delta J_{23})]/\sqrt{12} \tag{14b}$$

$$t_1 = [\delta J_{12} - \delta J_{34})]/\sqrt{2} \tag{15a}$$

$$t_2 = [\delta J_{13} - \delta J_{24})]/\sqrt{2} \tag{15b}$$

$$t_3 = [\delta J_{14} - \delta J_{23})]/\sqrt{2} \tag{15c}$$

The symmetry breaking T_2 and E distortions are illustrated in Figure 9. We have determined the eigenvalues and corresponding eigenstates of eq 12b by numerical diagonalization and studied the lowest of the resulting energies as a function of the distortion coordinates for each allowed value *S*. The resulting potential energy surfaces for $S = 0$ in the E space and $S = 4$ in a two-dimensional section of the T_2 space are shown in Figure 10. Both the E and T_2 modes are Jahn–Teller active in the $S = 1, 2, \ldots, 7$ spaces. The space of maximum spin, $S = 8$, is inactive with respect to both the E and T_2 distortions, and the $S = 0$ space exhibits only E distortions. The minima for a given distortion symmetry are degenerate, three-fold for E and four-fold for T_2. Depending on their relative energies, these minima are either global or local minima of the potential energy surfaces defined in the six dimensional distortion space. The minima correspond to core structures with symmetry lower than T_d. The symmetry breaking is spontaneous and results from first-order interactions between the degenerate states of given spin *S* that are generated by changes in the exchange parameters induced by geometrical distortions of the cluster. In the following two sections we discuss the structures, spin states, and energies at the minima of the potential energy surfaces for T_2 and E.

4.2. T_2 distortions

The four degenerate minima of the potential energy surface for the ground state in the T_2 space are located at the vertices of a equilateral tetrahedron (Figure 11, left). The symmetry of the cluster at the minima is C_{3v}. The three-fold axis runs through one of the four irons (called here the unique site); the remaining three sites are interchangeable by the C_3 operation. The six exchange-coupling constants at the T_2 minima are partitioned in two sets of three. For example, in the minimum for which Fe_4 is the unique site, there are two exchange-coupling constants, namely $J = J_{14} = J_{24} = J_{34}$ and $J' = J_{12} = J_{13} = J_{23}$ with $J' < J$. The latter three coupling constants provide strong antiferromagnetic interactions between the unique site and the other three sites, which among themselves are coupled by weaker antiferromagnetic exchange or, perhaps, even by ferromagnetic exchange-coupling constants.[15] For $S = 4$, these exchange interactions yield a spin state in which the spins of the three equivalent sites are aligned antiparallel to the spin of the unique site, as observed experimentally. The spin ordering for each minimum is shown in Figure 11. Thus, for the $S = 4$ state, our theoretical model correctly predicts the 3:1 ratio as well as the ordering of the iron spins, resulting from spontaneous symmetry breaking. The energies and states at the minima can be expressed analytically for any value of S. Let us consider the case for which Fe_4 is the unique site. For $J_{14} = J_{24} = J_{34} = J$ and $J_{12} = J_{13} = J_{23} = J'$ the spin Hamiltonian in eq 7 can be diagonalized by first coupling the spins of the three equivalent sites to composite spin S_{123} ($\hat{\mathbf{S}}_{123} = \hat{\mathbf{S}}_1 + \hat{\mathbf{S}}_2 + \hat{\mathbf{S}}_3$), followed by a coupling of S_{123} to spin S_4 of the unique site to give total spin S. The spin quantum numbers fulfill the following triangular inequalities: $|S_1 - S_2| \leq S_{12} \leq S_1 + S_2$, $|S_{12} - S_3| \leq S_{123} \leq S_{12} + S_3$, and $|S_{123} - S_4| \leq S \leq S_{123} + S_4$. As an example, we have listed in Table 3 the allowed values for S_{123} for $S = 4$, together with the number of multiplets for each value.

By using J and J' in eq 7 we obtain for the eigenstates the exchange energy

$$E(S, S_{123}) = \frac{1}{2} J\, S(S+1) + \frac{1}{2}(J' - J)\, S_{123}(S_{123}+1) - 3J - 9J' \tag{16}$$

Substitution of $J = J° + \Delta J$ and $J' = J° - \Delta J$ into eq 16 and addition of the elastic energies for the six Fe–Fe pairs then yield the total energy

$$E_T(S, S_{123}, \delta J) = E^0(S) + \Delta E_T(S, S_{123}, \delta J) = J° \left\{ \tfrac{1}{2} S(S+1) - 12 + \left[\tfrac{1}{2} S(S+1) - S_{123}(S_{123}+1) + 6 \right] \delta J + 6\kappa_T \delta J^2 \right\} \tag{17}$$

Given that the $S_{123}(S_{123} + 1)$ term has a negative sign, the lowest energy is attained for maximum value of S_{123} that is allowed for the given value of S ($S_{123}^{\max}$, see Table 4).

The energy minimum of $E_T(S, S_{123}^{\max}, \delta J)$ as a function of δJ is obtained for

$$\delta J_T^{\min}(S) = -\frac{\frac{1}{2} S(S+1) - S_{123}^{\max}\left(S_{123}^{\max}+1\right) + 6}{12\kappa_T} \tag{18}$$

The values of the numerator of eq 18 are listed as a function of S in the third column of Table 4. The corresponding minimum in T_2 space is located at $-\delta t_1 = -\delta t_2 = \delta t_3 = \sqrt{2}\delta J_T^{\min}$. The expression for the energy at the minimum is obtained by substitution of eq 18 into eq 17

$$E_{\mathrm{T}}^{\min}(S) = E_{\mathrm{T}}\left(S, S_{123}^{\max}, \delta J_{T}^{\min}(S)\right) = E^{\circ}(S) + \Delta E_{\mathrm{T}}(S) \tag{19}$$

In the third part of eq 19, the energy is expressed as the sum of the exchange energy of the undistorted cluster (eq 8) and a distortion-related energy

$$\Delta E_{\mathrm{T}}(S) = \Delta E_{\mathrm{T}}\left(S, S_{123}^{\max}, \delta J_{\mathrm{T}}^{\min}(S)\right) \tag{20a}$$

In units of J°, the energy in eq 20a can be expressed as

$$\frac{\Delta E_{\mathrm{T}}(S)}{J^{\circ}} = \frac{2\left(12\kappa_{\mathrm{T}}\delta J_{\mathrm{T}}^{\min}(S)\right)^{2}}{48\kappa_{\mathrm{T}}} \tag{20b}$$

The values of the numerator of the energy in eq 20b are listed as a function of S in the fourth column of Table 4. While $S = 0$ and $S = 8$ are T_2 inactive, the largest activity for this mode is found for $S = 4$, which allows this state to become the ground state (see below). In our treatment the spin ordering of the T_2 minimum for $S = 4$ is a consequence of the theoretical model and is not imposed as in the pioneering broken-symmetry DFT calculations for $M_S = 4$ state of the all-ferrous cluster by Torres et al.[16] Our results differ further in that the structure of the Fe–S core is predicted to have a three-fold axis while this symmetry is absent in the DFT optimized structure.

4.3 E distortion

The three degenerate minima of the potential energy surface for the ground state in the E space are located at the vertices of an equilateral triangle (Figure 11, right). The symmetry of the cluster at the minima is D_{2d}. The six exchange-coupling constants at the E minima are partitioned in two sets. For example, $J_{13} = J_{14} = J_{23} = J_{24} = J$ and $J_{12} = J_{34} = J'$ with $J > J'$ at the minimum on the e_{θ} axis. The latter two coupling constants provide weaker antiferromagnetic interactions (or ferromagnetic) interactions inside two disjoint pairs and stronger antiferromagnetic interactions between the two pairs. The Hamiltonian in eq 7 can be diagonalized analytically by first coupling the spins of the disjoint pairs to give pairs with spin S_{12} and S_{34} ($\hat{\mathbf{S}}_{12} = \hat{\mathbf{S}}_1 + \hat{\mathbf{S}}_2$ and $\hat{\mathbf{S}}_{34} = \hat{\mathbf{S}}_3 + \hat{\mathbf{S}}_4$), followed by a coupling of the pair spins to give resultant spin S. The spin quantum numbers fulfill the following triangular inequalities: $|S_1 - S_2| \le S_{12} \le S_1 + S_2$, $|S_3 - S_4| \le S_{34} \le S_3 + S_4$, and $|S_{12} - S_{34}| \le S \le S_{12} + S_{34}$. The energies of the eigenstates of eq 7 can be written as

$$E(S, S_{12}, S_{34}) = \frac{1}{2}JS(S+1) + \frac{1}{2}(J' - J)\{S_{12}(S_{12}+1) + S_{34}(S_{34}+1)\} - 12J' \tag{21}$$

Substitution of $J = J^{\circ} + \frac{1}{2}\Delta J$ and $J' = J^{\circ} - \Delta J$ into eq 21 and addition of the elastic energies for the six Fe–Fe pairs gives for the total energy the expression

$$E_{\mathrm{E}}(S, S_{12}, S_{34}, \delta J) = E^{\circ}(S) + \Delta E_{\mathrm{E}}(S, S_{12}, S_{34}, \delta J) = J^{\circ}\left\{\tfrac{1}{2}S(S+1) - 12 + \left[\tfrac{1}{4}S(S+1) - \tfrac{3}{4}\{S_{12}(S_{12}+1) + S_{34}(S_{34}+1)\} + 12\right]\delta J + 3\kappa_{\mathrm{E}}\delta J^2\right\} \quad (22a)$$

For any value of S, the lowest energy is obtained for the maximum value of the intermediate spins, $S_{12} = S_{34} = 4$. Substitution of these values into eq 22a yields eq 22b

$$E_{\mathrm{E}}(S, \delta J) = E^{\circ}(S) + \Delta E_{\mathrm{E}}(S, \delta J) = J^{\circ}\left\{\tfrac{1}{2}S(S+1) - 12 + \left[\tfrac{1}{4}S(S+1) - 18\right]\delta J + 3\kappa_{\mathrm{E}}\delta J^2\right\} \quad (22b)$$

The energy minimum of $E_{\mathrm{E}}(S, \delta J)$ is obtained at

$$\delta J_{\mathrm{E}}^{\min}(S) = \frac{36 - \frac{1}{2}S(S+1)}{12\kappa_{\mathrm{E}}} \quad (23)$$

The corresponding minimum in E space is located at $\delta e_{\theta} = -\sqrt{3}\delta J_{E}^{\min}$ and $\delta e_{\varepsilon} = 0$. The expression for the energy at the minimum is obtained by substitution of eq 23 into eq 22b

$$E_{\mathrm{E}}^{\min}(S) = E_{\mathrm{E}}\left(S, \delta J_{\mathrm{E}}^{\min}(S)\right) = E^{\circ}(S) + \Delta E_{\mathrm{E}}(S) \quad (24)$$

where we have used the definition

$$\Delta E_{\mathrm{E}}(S) = \Delta E_{\mathrm{E}}\left(S, \delta J_{\mathrm{E}}^{\min}(S)\right) \quad (25a)$$

In units of J°, the energy in eq 25a can be expressed as

$$\frac{\Delta E_{\mathrm{E}}(\mathrm{S})}{J^{\circ}} = -\frac{\left(12\kappa_{\mathrm{E}}\delta J_{\mathrm{E}}^{\min}(S)\right)^2}{48\kappa_{\mathrm{E}}} \quad (25b)$$

The values of the numerators of eqs 23 and 25b have been listed as a function of S in Table 5. The E activity is largest for $S = 0$, decreases with increasing values of the spin, and eventually vanishes for $S = 8$. A comparison of Tables 4 and 5 shows that $\kappa_{\mathrm{T}}\delta J_{\mathrm{T}}^{\min}(S) = \kappa_{\mathrm{E}}\delta J_{\mathrm{E}}^{\min}(S)$ and $\kappa_{\mathrm{T}}\Delta E_{\mathrm{T}}(S) = 2\kappa_{\mathrm{E}}\Delta E_{\mathrm{E}}(S)$ for $S > 3$.

4.4. Relative energies of minima

In this section we analyze the relative energies of the T_2 and E minima for the nine spin states of the all-ferrous cluster.[17] In particular, we present for each value of S the condition for which the T_2 minimum is below the E minimum, the conditions for the level crossings between the T_2 minimum for $S = 4$ and the T_2 minima for $S < 4$, and finally the condition for which the T_2 minimum for $S = 4$ is the absolute minimum. The T_2 minimum for spin S is lower in energy

than the E minimum for the same value of the spin provided $|\Delta E_T(S)| > |\Delta E_E(S)|$. The inequality implies that the force constants for T_2 and E satisfy the condition $\kappa_T/\kappa_E < q_S$, with q_S being the value given in Table 6. Since $S = 0$ is T_2 inactive, the E minimum is lowest for any finite value of κ_E. For $S = 1$ to 4 the condition is fulfilled for increasingly larger values for κ_T/κ_E (N.B. In general, a large force constant implies a small distortion (energy). Thus, a higher q_S value signifies an increased propensity for the T_2 minimum to be lowest.)

Above we mentioned that the largest T_2 stabilization energy, $|\Delta E_T(S)|$, is attained for $S = 4$ (Table 4). In the limit $\kappa_T \rightarrow \infty$, where the distortion energies vanish for all values of S, the $S = 4$ energy is greater than the energies for $S = 0 - 3$ (eq 8). By lowering the value for κ_T, the energy of the T_2 minimum for $S = 4$ energy drops relative to those for the other spin states and consecutively crosses the energies of the T_2 minima for $S = 3$, 2, 1, and 0 at the values $\kappa_T = p_S$ listed in Table 7. We note that the p_S values are an increasing function of S. Thus, if the condition for the crossing with $S = 0$ ($\kappa_T < 2.817$, Table 7) is fulfilled, then the T_2 minimum for $S = 4$ has the lowest energy of all T_2 minima. The crossing with $S = 0$ considered here is with an undistorted level as $S = 0$ is T_2 inactive (Table 4).

Since the exchange energy of the unperturbed cluster, $E°(S)$, and the E stabilization energy, $|\Delta E_E(S)|$, are increasing and decreasing functions of spin quantum number S, respectively (Table 5), the energy at the E minima, $E_E^{min}(S)$, is an increasing function of S. Thus, the E minimum for $S = 0$ is among the E minima the lowest in energy for any value for κ_E. Hence, the T_2 minimum for $S = 4$ is lower in energy than any of the E minima, provided $E_T^{min}(S=4) < E_E^{min}(S=0)$. The latter condition implies an inequality for the ratio of the force constants for the T and E distortions,

$$\frac{\kappa_T}{\kappa_E} < \frac{169 - 60\kappa_T}{162} \tag{26}$$

In the limit $\kappa_E \rightarrow \infty$ (where the E distortion for $S = 0$ vanishes) the condition reduces to the condition $\kappa_T < p_{S=0}$ which ascertains that the T_2 minimum for $S = 4$ is lower in energy than the one for $S = 0$ (Table 7). Having established that the T_2 minimum for $S = 4$ is lower in energy than (i) all E minima and (ii) all T_2 minima for $S \neq 4$, it follows that eq 26 is the condition which ensures that the T_2 minimum for $S = 4$ is the absolute energy minimum of the all-ferrous cluster. Finally, it can be shown that if the absolute minimum is a T_2 minimum, then it must be the T_2 minimum for $S = 4$. Thus, the absolute minimum is either the T_2 minimum for $S = 4$ or the E minimum for $S = 0$. The latter minimum is the absolute minimum if the condition in eq 26 is violated. The origin of the differences in the force constants required for the stabilization of the T_2 minimum is the subject of a separate study.

These conditions described in this section have a number of corollaries:

- **a.** The largest value of κ_T/κ_E for which the T_2 minimum for $S = 4$ is the ground state is $^{169}/_{162} \approx 1.04$. Thus, κ_T must typically be smaller than κ_E ($\kappa_E \approx 1.04\ \kappa_E > \kappa_T$) to obtain an $S = 4$ ground state. Thus, under this condition the electronic state at the absolute energy minima is similar to the "3:1", $S = 4$ state inferred from spectroscopic analysis of the all-ferrous clusters in complex **1** and *Av*2.
- **b.** For $\kappa_T/\kappa_E = 1$, eq 26 implies $\kappa_T < {}^{7}/_{60}$ and $\Delta J > {}^{130}/_{7}\ J°$. Thus, in the case of equal force constants, the force constant for T_2 must be small and the change in J very large in order to obtain an $S = 4$ ground state.

c. To obtain a T_2 minimum for $S = 4$ with vanishing coupling constants between the three equivalent sites ($J' = 0$) requires that $\delta J_T^{min}(S=4) = 1$. This condition and the expression $\kappa_T \delta J_T^{min}(S=4) = {}^{13}/_6$ (Table 4) yield the value $\kappa_T = {}^{13}/_6 \approx 2.167$. Substitution in eq 26 yields the condition $\kappa_E > 9$ for ensuring that the T_2 minimum for $S = 4$ is the absolute minimum. For $J' > 0$ (J' antiferromagnetic) the T_2 minimum for $S = 4$ is the absolute minimum if ${}^{13}/_6 < \kappa_T < {}^{169}/_{60}$ and $\kappa_E > \kappa_E^{lim} = 162\kappa_T / (169 - 60\kappa_T)$; the limiting value for κ_E varies as a function of κ_T in the range $9 < \kappa_E^{lim} < \infty$. For $J' < 0$ (J' ferromagnetic) the T_2 minimum for $S = 4$ is the absolute minimum if $\kappa_T < {}^{13}/_6$ and $\kappa_E > \kappa_E^{lim}$; the limiting value for κ_E varies as a function of κ_T in the range $0 < \kappa_E^{lim} < 9$.

d. The upper limit of κ_T (${}^{169}/_{60}$, eq 26) and lower limit for $\delta J_T^{min}(S=4)$ (${}^{13}/_6 / \kappa_T = {}^{10}/_{13}$) for which the T_2 minimum for $S = 4$ remains the absolute minimum are reached in the limiting case $\kappa_E \rightarrow \infty$. For these values we obtain the largest possible value for $J' = J^\circ[1 - \delta J_T^{min}(S=4)] = {}^{3}/_{13} J^\circ \approx 0.231\ J^\circ$ consistent with an absolute T_2 minimum of $S = 4$. In this limit, we find that $J = J^\circ[1 + \delta J_T^{min}(S=4)] = {}^{23}/_{13} J^\circ \approx 1.769\ J^\circ$ and $J'/J = {}^{3}/_{23} \approx 0.13$. Smaller values for the J'/J ratio, including negative values arising from ferromagnetic J' values, are found away from the limit.

5. Application of theoretical model to all-ferrous clusters

5.1 Unique sites in the all-ferrous clusters of complex 1 and Fe-protein

Given certain core-specific conditions on the force constants, we identified in the previous section a "3:1", $S = 4$ state as the ground state of the all-ferrous cluster on the basis of a theoretical analysis that completely ignores external perturbations and exclusively focuses on the $[4Fe–4S]^0$ core. The intrinsic (core-specific) nature of this solution suggests why the same ground state is present in both complex **1** and the protein-bound all-ferrous cluster of *Av*2, in spite of significant differences in their terminal coordination. Thus, the present study strongly suggests that the "3:1", $S = 4$ ground state of the all-ferrous *Av*2 cluster is not imposed on the cluster by changes in the exchange-coupling constants induced by the protein environment, as suggested in an earlier study,[8] but is an intrinsic property of the cluster core. The magneto–structural correlation between J and the metal–ligand–metal angle, notably the increase in the value for J as a function of this angle, frequently observed in series of structurally related transition metal complexes,[15] suggests that the antiferromagnetic couplings in the Fe–S–Fe bridges of the all-ferrous cluster become larger when the bond angles are increased. Thus, we predict that the angles $Fe_i–S_k–Fe_j$ the angles for i = 1, 2, 3 and j = 4 (i.e., for bridges between one of the equivalent sites and the unique site) are larger than for i, j = 1, 2, 3 (i.e., for bridges between the three equivalent iron sites). The prediction is confirmed by the data for these angles listed in Table 8. Indeed, in both the protein-bound cluster and complex **1**, the former angles are > 70° with an average 71.9° and the latter angles are < 70° with an average of 67.8°. The remarkable agreement in the angular values for the two clusters (see Table 8) corroborates the intrinsic (core-based) nature of the forces shaping the core conformation. In the labeling adopted in Table 8, the unique site is designated as Fe_4 both in complex **1** and the all-ferrous cluster of the Fe-protein. The unique site (Fe_4 in our numbering) appears in PDB file 1G1M,[7] containing the structure of the all-ferrous Fe-protein of *A. vinelandii*, as iron site Fe(3), which is one of the two solvent exposed irons of the cluster. A complete correspondence list is given in footnote b of Table 8. The Fe–Fe distances show the same trend as the bond angles (see Table S2), with the Fe_4-Fe_i (i = 1–3) distances being on the average 0.15 / 0.10 Å (Fe-protein / complex **1**) shorter than the $Fe_i–Fe_j$ (i, j = 1–3) distances. Concomitantly, the diagonal distances

for the unique sites, Fe_4–S_4 = 4.090 / 4.059 Å (Fe-protein / complex **1**) are 0.24 / 0.17 Å longer than the Fe_i–S_i (i = 1–3) distances for the three equivalent sites $<Fe_i–S_i>_{avg}$ = 3.853 / 3.866 Å. Thus, we have succeeded to assign the unique *spectroscopic* iron site, identified in the all-ferrous Fe-protein by Yoo et al.,[6] to a specific *structural* site in the crystallographic structure of the cluster (Figure 12). Similarly, we have identified the unique site in the Mössbauer spectra of complex **1** (Figures 3, 5) to site Fe_4 in its structure (Figure 1).

The unique sites in the all-ferrous clusters of complex **1** and Fe-protein can also be identified by comparing the cluster cores in these systems. Table 9 presents a list containing all 12 possible overlays of the two cluster cores together with the resulting RMSDs for Fe-only as well as 4Fe–4S based minimizations. Using our atom labeling, mappings that assign site Fe_4 of the Fe-protein cluster to site Fe_4 of complex **1** give consistently the lowest three RMSDs (indicated in bold face), confirming that Fe_4 is the unique site in both systems. Accordingly, interchanges of the equivalent sites, Fe_1, Fe_2, and Fe_3, obtained by applying the pseudo C_3 symmetry operator, produce only minor changes in the RMSDs. The first overlay of Table 9 (case 1) is shown in Figure 13 and reveals a remarkable degree of congruence between the two cluster cores. Given the rather low resolution (2.25 Å) of the all-ferrous Fe-protein structure, it may seem unlikely that it is feasible to identify the unique site in the x-ray structure. However, it should be noted that the Debye–Waller factors of the core atoms are about half the protein average, implying that the core structure is much better defined than the overall protein structure. Strop et al.[7] concluded from the low Debye–Waller factors that the crystallographic cluster structure pertains to a single conformation, as it is implicitly assumed in our analysis, and not to a conformational superposition. In this respect, not surprisingly, the protein environment cannot be entirely dismissed, as it apparently locks the cluster core into one of its intrinsic minima.

5.2. Is there experimental evidence for E, *S* = 0 minima in all-ferrous clusters?

The spectroscopic and structural evidence discussed so far support the presence of T_2, $S = 4$ minima in the all-ferrous clusters of two systems, *viz.* complex **1** and the Fe-protein from *A. vinelandii*. Some literature data raise the possibility that all-ferrous clusters may also appear in the alternative E, $S = 0$ minima. In a report of an EXAFS study of the Ti(III) citrate-reduced all-ferrous cluster in the Fe-protein of *A. vinelandii*, the iron–iron distances appear in two sets, one consisting of two long distances and the other of four short distances.[18] These distances are consistent with the D_{2d} symmetry of the E minima. However, such an assignment appears to be baseless taking into consideration the following points: (1) Mössbauer studies of Ti(III) citrate-reduced Fe-protein unambiguously show that the all-ferrous cluster has an $S = 4$ ground state rather than the $S = 0$ state predicted for the E minimum. (2) Given the magneto–structural correlation between exchange-coupling constant and bridging angle, the E minimum is predicted to have a cluster structure with two short and four long iron–iron distances rather than two long and four short distances as inferred from the EXAFS data. (3) The analysis described in the EXAFS report assumes that all iron sites are equivalent, precluding the identification of core conformations with inequivalent sites, such as the C_{3v} symmetric T_2 conformation. (4) A reversal in the energy order of the T_2 and E minima would require significant changes in the force constants for these, otherwise remarkably conserved (Figure 13), core units. In a recent EPR and magnetic susceptibility study of flavodoxin hydroquinone (E_m = −515 mV) treated *Av*2, the iron–sulfur cluster was reported to be in an all-ferrous, $S = 0$ state.[9] This claim, however, has not yet been substantiated by application of a technique sensitive to the oxidation state of the cluster and should, given point (4) and the high potential at which the state was generated, be viewed with caution.

5.3. Graphical comparison of cores in complex 1 and *Av2*

In Figures S2A and S2B of the Supporting Information we have presented graphical comparisons of the Fe–Fe distances (Table S2) and Fe–S–Fe angles (Table 8) of the all-ferrous cores in **1** and *Av*2. In section 5.1 it was shown that the 12 Fe–S–Fe bridge angles can be cast in two sets: a set of 6 small angles for bridges between the equivalent irons (set 1) and a set of 6 large angles for bridges between the unique site and the equivalent sites. Accordingly, the six Fe–Fe distances can be cast in sets of 3 short distances (set 1) and 3 long distances (set 2). While the angles or distances belonging to one set are predicted by our model to be equal, examination Table S2 and Table 8 reveals that the sets contain different values. The widths of the dispersion ranges for each set can be gleaned from Figures S2A (and S2B): for set 1 the widths are 0.07 Å (2.7°) in complex **1** and 0.11 Å (5.4°) in *Av*2; for set 2 the spreads are 0.05 Å (2.2°) in complex **1** and 0.12 Å (3.3°) in *Av*2. The averages for the sets have been indicated by dashed arrows in the figures and are separated by 0.10 Å (3.6°) in complex **1** and by somewhat higher values, 0.15 Å (4.6°), in *Av*2. The set widths are smaller than the separations between the set averages in complex **1** and of similar magnitude in *Av*2. Interestingly, the two clusters exhibit the same correlation between the distances of the two sets: the shortest distance of set 1 (Fe_1–Fe_2 in **1** and Fe_2–Fe_3 in *Av*2) and the longest distance of set 2 (Fe_3–Fe_4 in **1** and Fe_1–Fe_4 in *Av*2) belong to complementary iron pairs; analogously, the intermediate distance of set 1 (Fe_2–Fe_3 in **1** and Fe_1–Fe_2 in *Av*2) and the intermediate distance of set 2 (Fe_1–Fe_4 in **1** and Fe_3–Fe_4 in *Av*2) and the longest distance of set 1 (Fe_1–Fe_3 in **1** and Fe_1–Fe_3 in *Av*2) and the shortest distance of set 2 (Fe_2–Fe_4 in **1** and Fe_2–Fe_4 in *Av*2) belong to complementary pairs as well (see Figure S2A). A similar correlation exists for Fe–S–Fe angles (see Figure S2B). In terms of symmetrized coordinates, the correlation indicates that the core structures of the two clusters are predominantly distorted in T_2 space. However, since the three complementary pairs of Fe–Fe distances in Figure S2A are separated by different distances, the cluster locations in T_2 space are displaced with respect to the diagonal positions of the T_2 minima shown in Figure 11 (left). The qualitative similarity of the distortions in **1** and *Av*2 suggests that it is an intrinsic property of the core unit, although the amplitudes of the distortions differ between the two clusters (Figure S2), implying that the intrinsic distortional forces have been modulated by the changes in terminal ligation or cluster environment. We anticipate that a full understanding of these distortions will require an extension of the model presented in this paper by taking explicitly the 3d orbital states of the irons and their relationship to the exchange interactions between the irons into consideration. The distortions are partly reproduced by the DFT calculations for the broken-symmetry configuration representing the $S = 4$ state of *Av*2 by Torres et al.,[16] who obtained a layered structure in which the 6 Fe–Fe distances appear as 1 short distance, 4 equal intermediate distances, and 1 long distance, with the short and long distances connecting complementary iron pairs and the unique site belonging to the long-distance pair. Thus, the structure obtained by Torres et al. shows also a distortion in T_2 space but one that, unlike the T_2 minima of Figure 11, is located on a t_i axis. This prediction differs from the X-ray data for both **1** and *Av*2 in that the 4 intermediate Fe–Fe distances are equal and not dispersed over ranges with widths of ~0.1 Å as in the X-ray structures (Figure S2A). Torres et al. reported also DFT calculations for the broken-symmetry configuration representing the $S = 0$ state and found that, while this state is lower in energy than the broken-symmetry $S = 4$ state in gas phase, the "$S = 4$" state becomes lowest by a wide margin of ~2000 cm^{-1} when the cluster is placed in a protein/solvent simulating environment, suggesting an essential role of the protein in the stabilization of the $S = 4$ state. In contrast, our analysis of complex **1** shows that the $S = 4$ ground state of the all-ferrous core is also accessible in the absence of a hydrogen bonding protein/water environment, adding support to the idea that the $S = 4$ ground state is an intrinsic property of the core.

Supplementary Material

Refer to Web version on PubMed Central for supplementary material.

Acknowledgments

This research was supported by NSF Grant MCB 0424494 to E.M. and NIH Grant GM 28856 to R.H.H.

References

1. Scott TA, Berlinguette CP, Holm RH, Zhou HC. Proc Natl Acad Sci USA 2005;102:9741–9744. [PubMed: 15985547]
2. Deng L, Holm RH. J Am Chem Soc 2008;130:9878–9886. [PubMed: 18593124]
3. Rao PV, Holm RH. Chem Rev 2004;104:527–559. [PubMed: 14871134]
4. Angove HC, Yoo SJ, Burgess BK, Münck E. J Am Chem Soc 1997;1997:8730–8731.
5. Angove HC, Yoo SJ, Münck E, Burgess BK. J Biol Chem 1998;273:26330–26337. [PubMed: 9756863]
6. Yoo SJ, Angove HC, Burgess BK, Hendrich MP, Münck E. J Am Chem Soc 1999;121:2534–2545.
7. Strop P, Takahara PM, Chiu HJ, Angove HC, Burgess BK, Rees DC. Biochemistry 2001;40:651–656. [PubMed: 11170381]
8. Hans M, Buckel W, Bill E. J Biol Inorg Chem 2008;13:563–579. [PubMed: 18274792]
9. Lowery TJ, Wilson PE, Zhang B, Bunker J, Harrison RG, Nyborg AC, Thiriot D, Watt GD. Proc Natl Acad Sci USA 2006;103:17131–17136. [PubMed: 17085583]
10. Münck E, Bominaar EL. Science 2008;321:1452–1453. [PubMed: 18787157]
11. Surerus KK, Hendrich MP, Christie PD, Rottgardt D, Orme-Johnson WJ, Münck E. J Am Chem Soc 1992;114:8579–8590.
12. Münck E, Surerus KK, Hendrich MP. Methods Enzymol 1993;227:463–479. [PubMed: 8255233]
13. Zimmermann R, Münck E, Brill WJ, Shah VK, Henzl MT, Rawlings J, Orme-Johmson WH. Biochim Biophys Acta 1978;537:185–207. [PubMed: 215215]
14. Dabrowski L, Piekoszewski J, Suwalski. Nucl Inst Methods 1971;91:93–95.
15. Kahn, O. Molecular Magnetism. Verlag-Chemie; New York: 1993. Willett, RD.; Gatteschi, D.; Kahn, O., editors. NATO ASI series, Series C: Mathematical and Physical Sciences. Vol. 140. Reidel Publishing; Dordrecht: 1985. Magneto–Structural Correlations in Exchange Coupled Systems.
16. Torres RA, Lovell T, Noodleman L, Case DA. J Am Chem Soc 2003;125:1923–1936. [PubMed: 12580620]
17. The force constant κ_A for the symmetric mode is assumed to be ∞.
18. Musgrave KB, Angove HC, Burgess BK, Hedman B, Hodgson KO. J Am Chem Soc 1998;120:5325–5326.

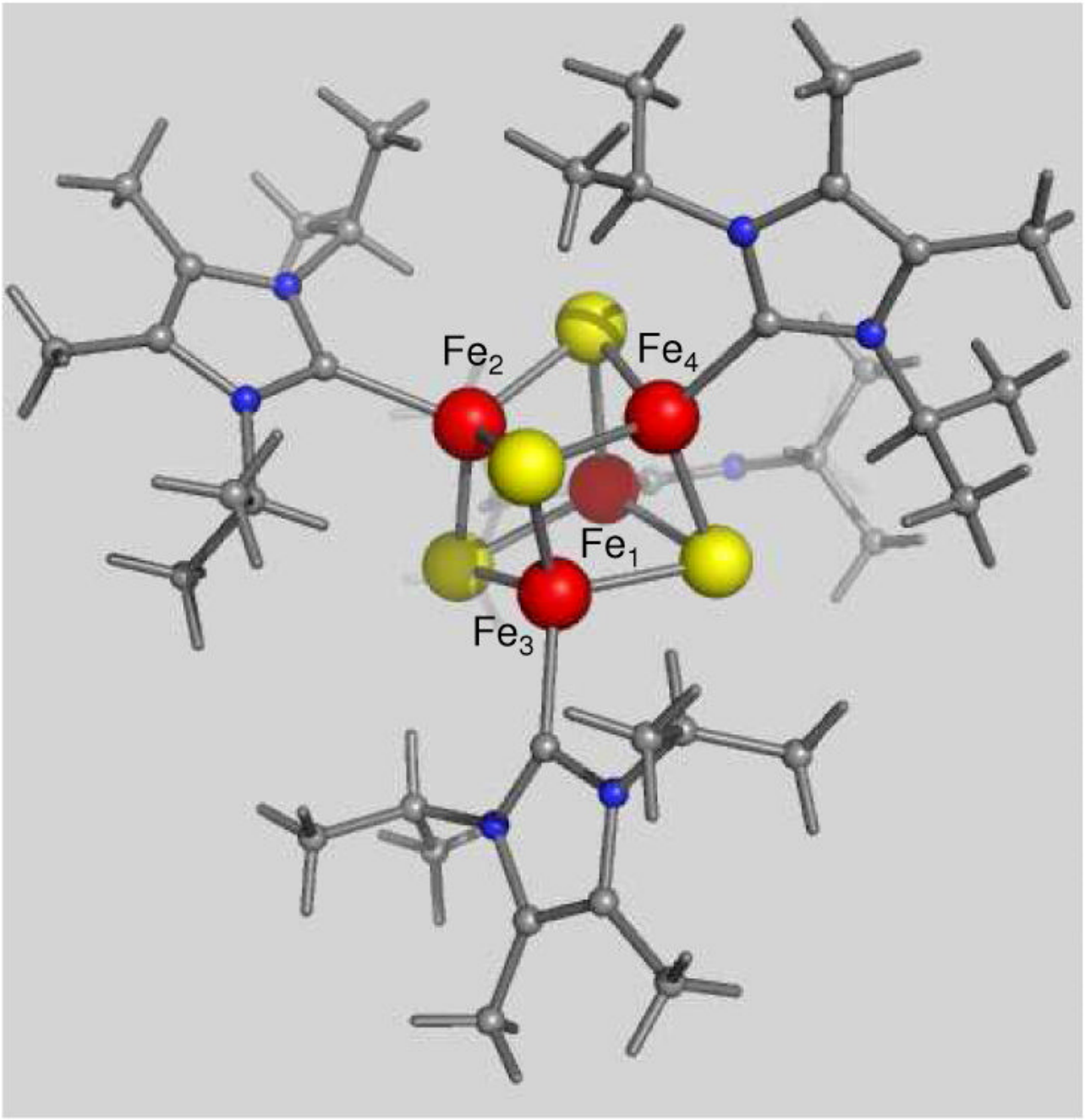

Figure 1.
Structure of $[Fe_4S_4(Pr^i_2NHCMe_2)_4]$.[2] Ranges and mean values (A) of core distances: Fe-S 2.291(1)-2.338(1), 2.33(2); Fe-Fe 2.603(1)-2.764(1), 2.68(6). The irons labeled Fe_1, Fe_2, Fe_3, and Fe_4 correspond with the irons Fe(1), Fe(3), Fe(4), and Fe(2) of [ref 2].

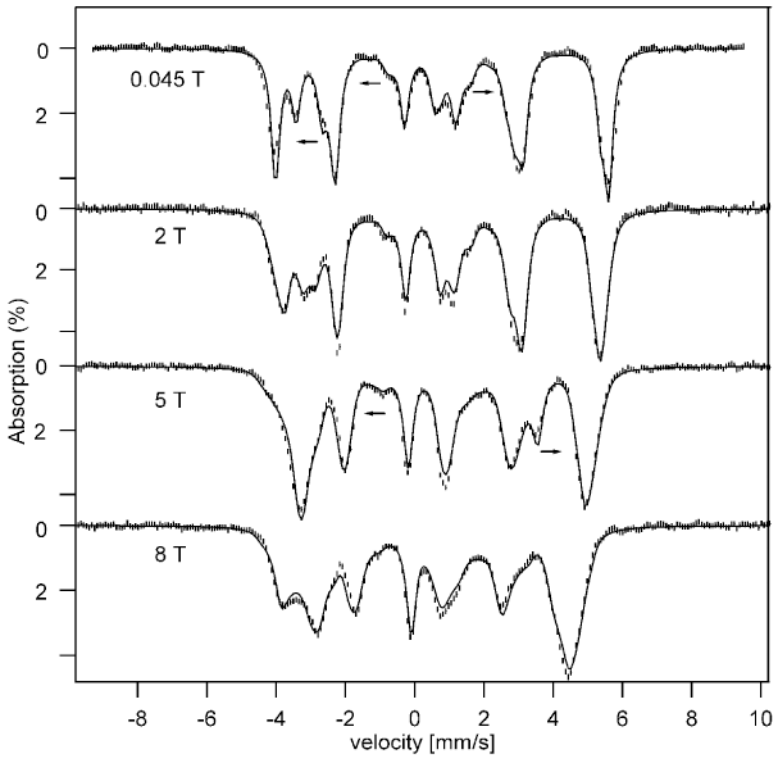

Figure 2.

4.2 K Mössbauer spectra of complex **1** recorded in the parallel applied magnetic fields indicated. The solid lines are simulations using the parameters quoted in Table 1. The arrows indicate the line displacements of the unique site upon increasing the magnetic field.

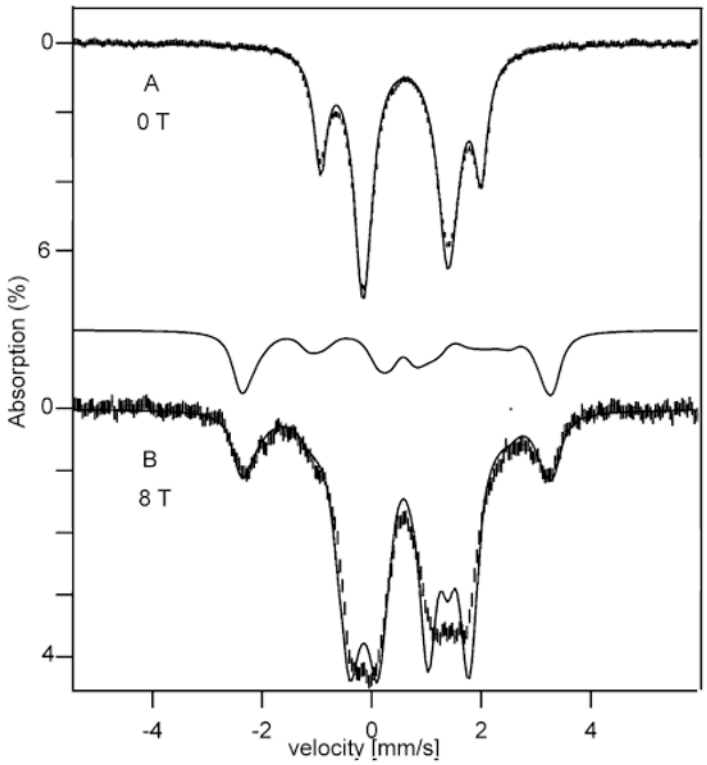

Figure 3.
100 K Mössbauer spectra of complex **1** recorded in zero field (A) and an 8.0 T field applied parallel to the γ beam (B). The solid lines are simulations using the parameters quoted in Table 1.

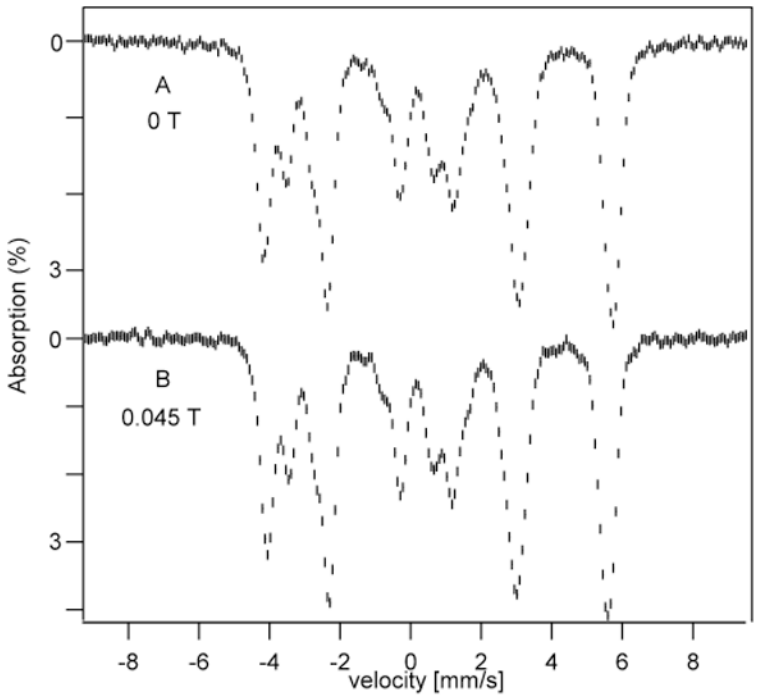

Figure 4.
4.2 K Mössbauer spectra of complex **1** recorded in zero field (A) and an 0.045 T field applied parallel to the γ beam (B).

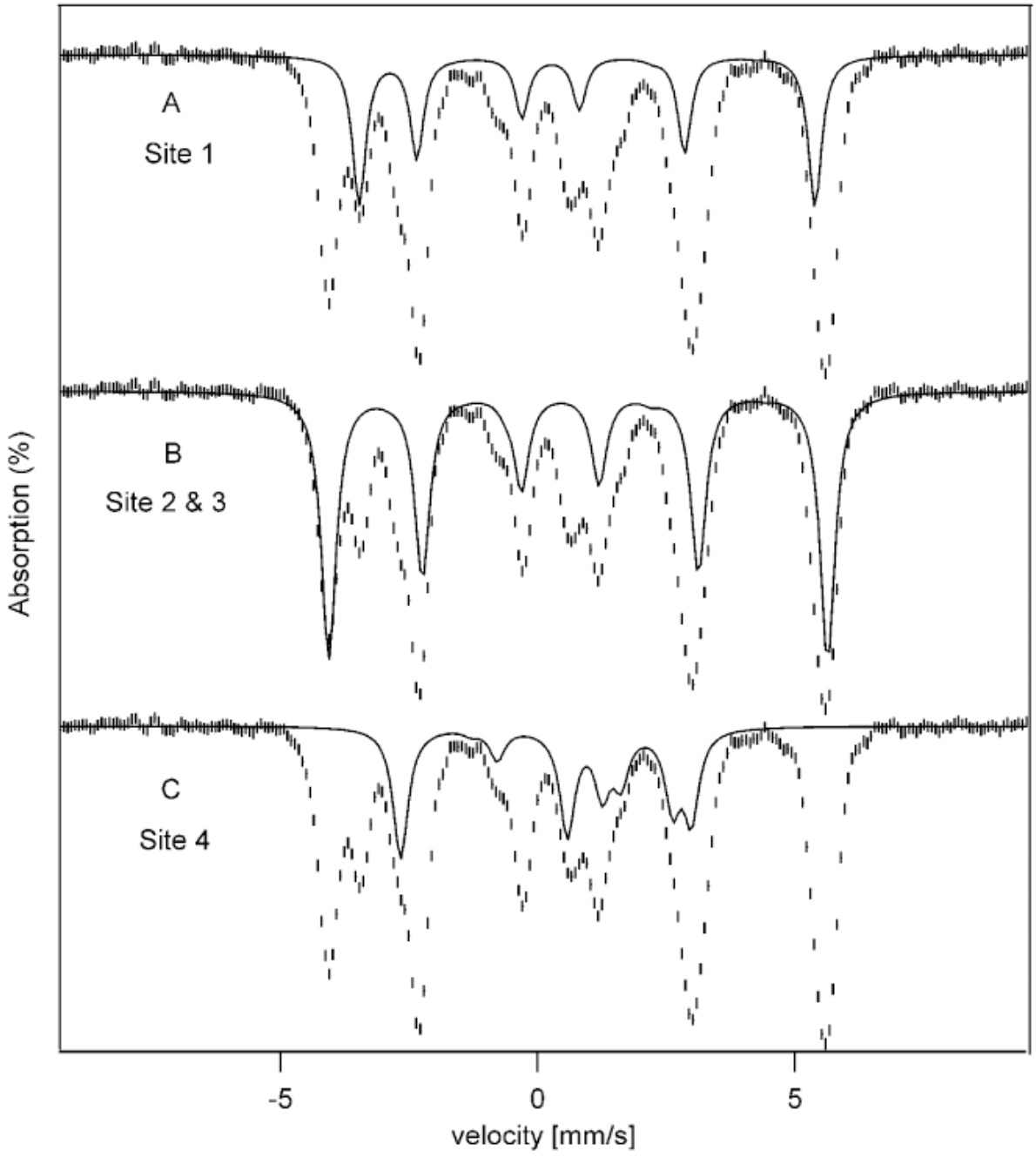

Figure 5.
4.2 K Mössbauer spectrum of complex **1** recorded in 0.045 T parallel applied magnetic field (same as in Fig. 2). Solid lines drawn through the data show the contributions of site 1 (A), site 2 & 3 (B) and site 4 (C).

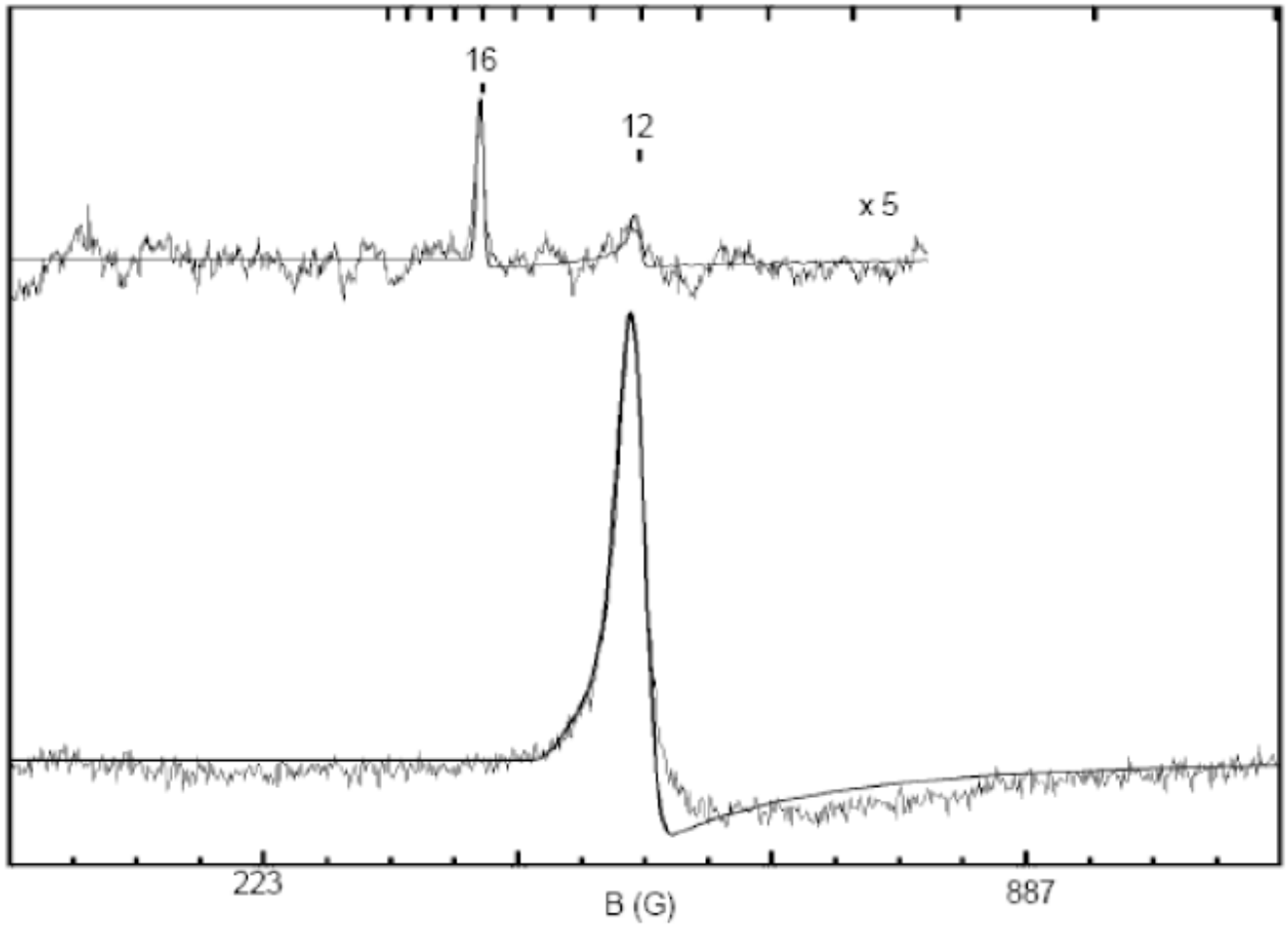

Figure 6.

X band parallel mode EPR spectra of complex **1** recorded at 2 K (*top*) and 8 K (*bottom*). Conditions: Frequency 9.27 GHz; microwave power 2 mW (*top*) and 0.2 mW (*bottom*); modulation 0.3 mT (*top*) and 1 mT (*bottom*). The solid lines drawn through the data are simulations, using SpinCount, for an $S = 4$ system with $D = -1.9$ cm^{-1}, $E/D = 0.07$ cm^{-1}, $\sigma_{E/D} = 0.03$, $g_x = g_y = 2$ and $g_z = 2.015$.

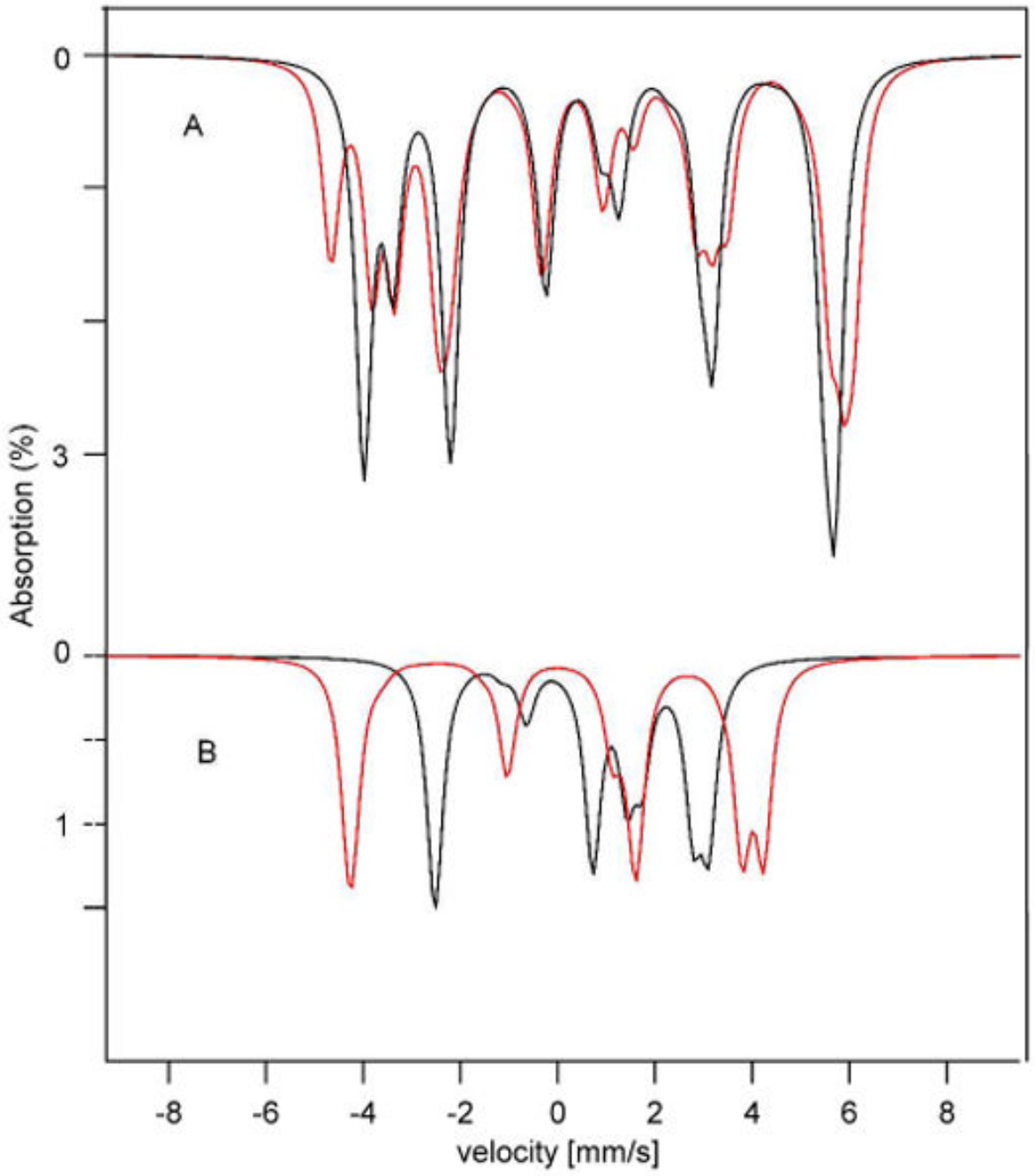

Figure 7.

(A) Simulated Mössbauer spectra (sum of sites 1-3) at 1.5 K, 0.045 T for the *Av*2 protein (red line) and at 4.2 K, 0.045 T complex **1** (black line). **(B)** Simulated Mössbauer spectra of site 4 at 1.5 K, 0.045 T for the *Av*2 protein (red line) and at 4.2 K, 0.045 T complex **1** (black line).

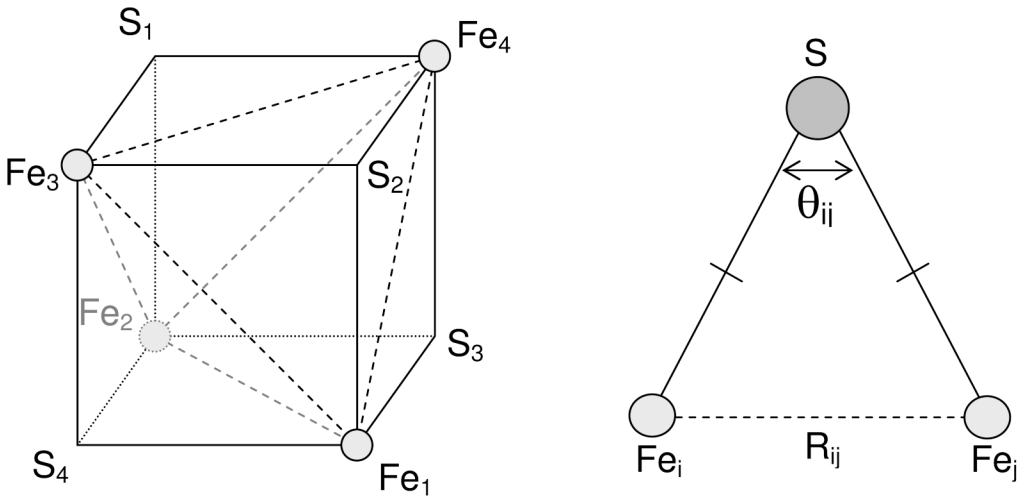

Figure 8.

(*left*) Schematic representation of the core of an iron–sulfur cluster, showing the labeling of the core atoms and the six iron-iron distances considered in the theoretical model. The sulfur atoms are located outside the cube spanned by the irons. (*right*) One of the iron–sulfur–iron bridges in the cluster, showing an iron–iron distance and the related bond angle.

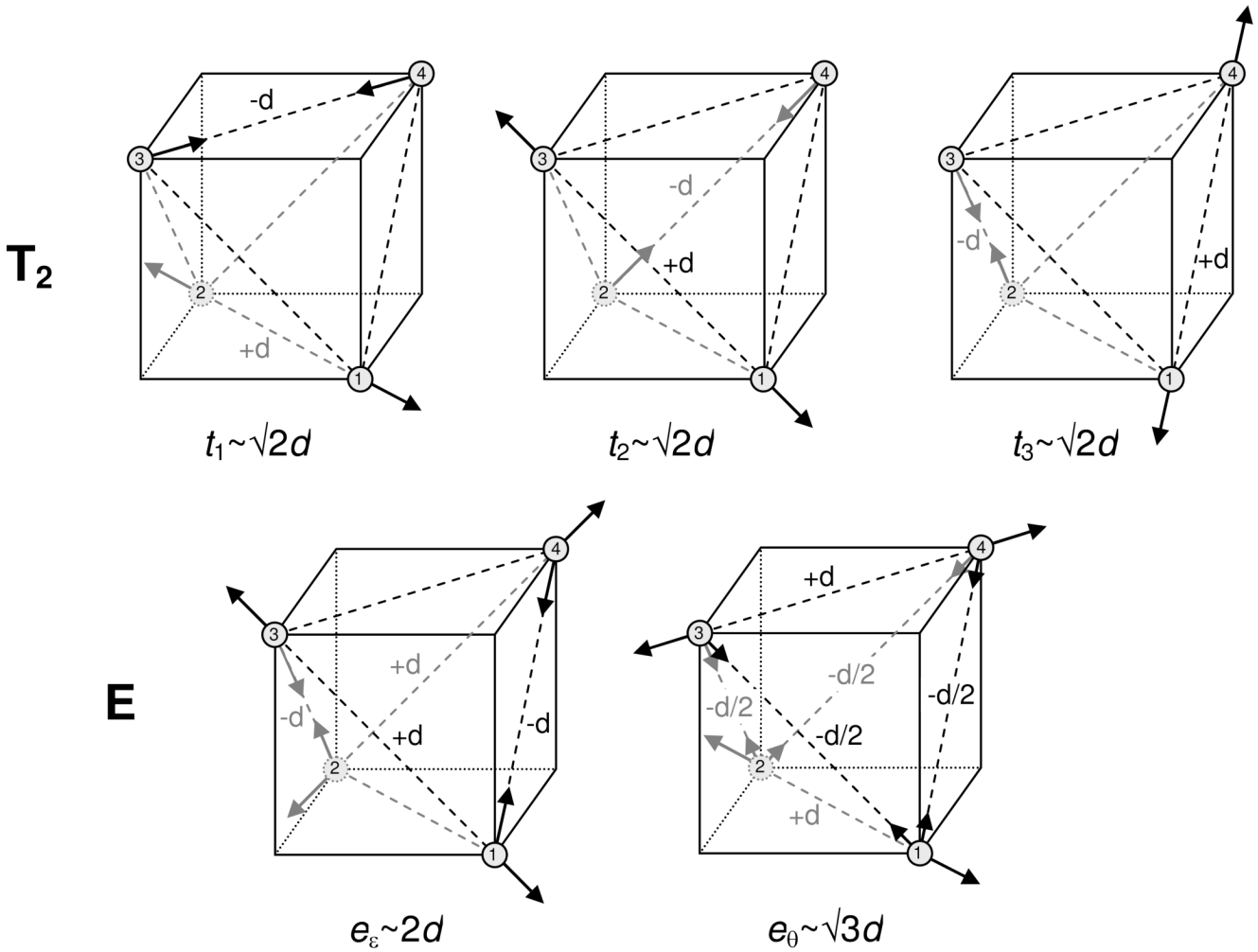

Figure 9.
Symmetrized distortion coordinates of T_2 and E symmetry, defined in eqs 14, 15, describing the changes in the iron–iron distances. The iron positions have been superimposed on a cube for visual guidance.

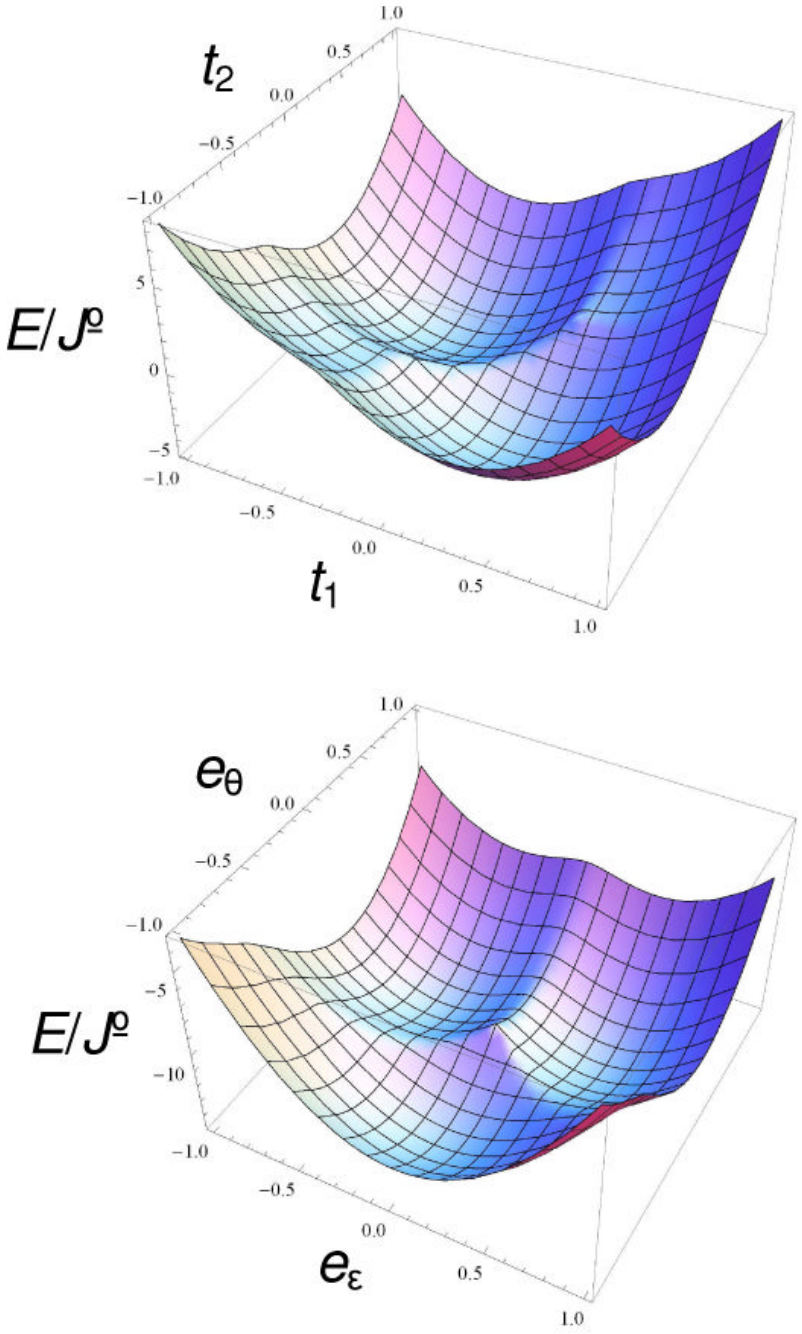

Figure 10.

(*top*) Two-dimensional section at $t_3 = -13\sqrt{2}/60 \approx 0.3064$ of the potential energy surface of the cluster for $S = 4$ and $\kappa_T = 10$ defined on the three-dimensional T_2 space, containing two of the four degenerate minima (see also Figure 11, left). (*bottom*) Potential energy surface of the cluster for $S = 0$ and $\kappa_E = 10$ defined on the two-dimensional E space, showing three degenerate minima (see also Figure 11, right).

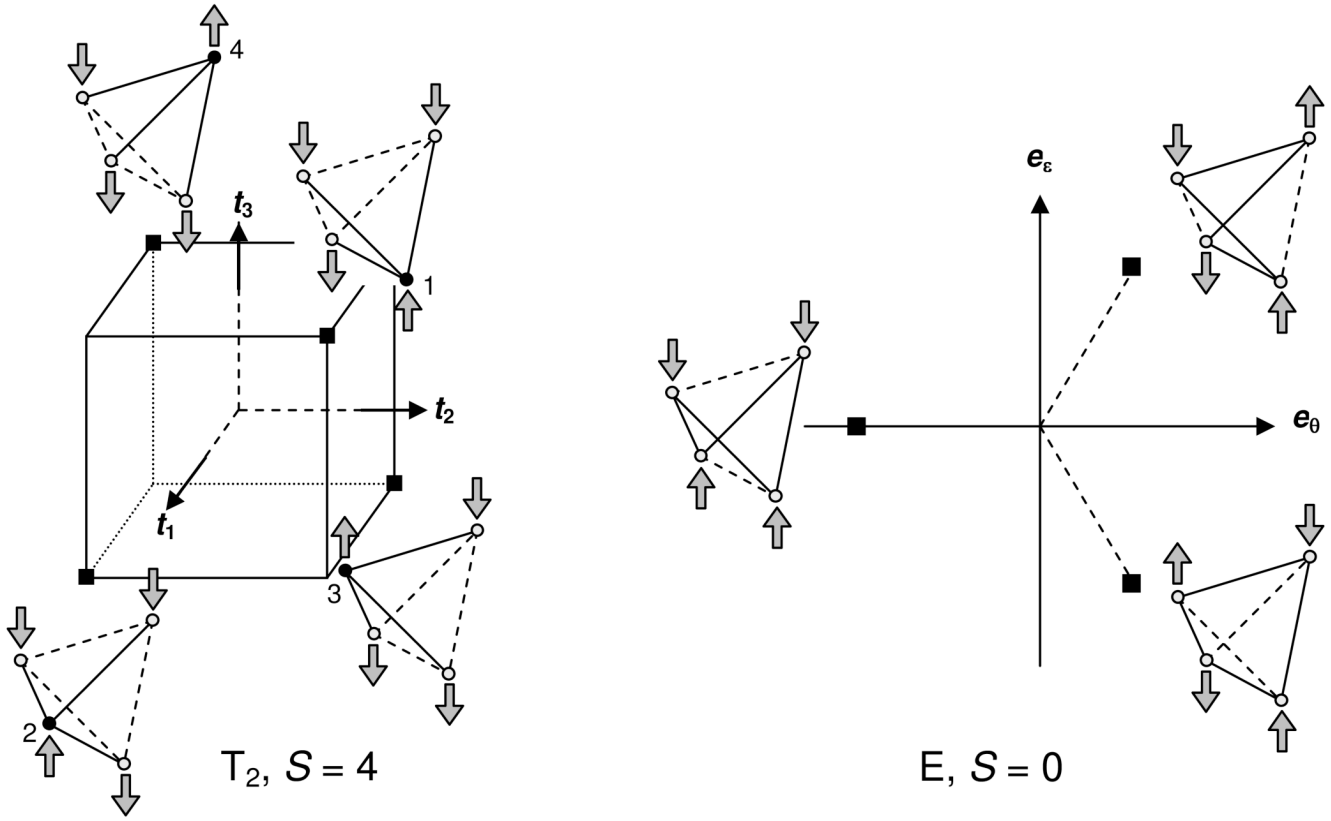

Figure 11.

(*left*) Schematic representation of the positions of the four degenerate energy minima (black squares) of the potential energy surface for the cluster in the three-dimensional T_2 space. The cube containing the equilateral tetrahedron with the locations of the minima has been indicated. The spin ordering of the irons for $S = 4$ is shown for each minimum. The solid and dashed lines in each cartoon connect iron pairs for which the exchange interactions are increased and decreased, respectively, as a result of the distortion. The unique site for each minimum has been indicated by a filled circle. (*right*) Schematic representation of the positions of the three degenerate energy minima (black squares) of the potential energy surface for the cluster in the two-dimensional E space. The minima are located on the vertices of an equilateral triangle. The spin ordering of the irons for $S = 0$ has been shown for each minimum. The solid and dashed lines in each cartoon connect iron pairs in which the exchange-coupling constants are increased and decreased, respectively, as a result of the distortion.

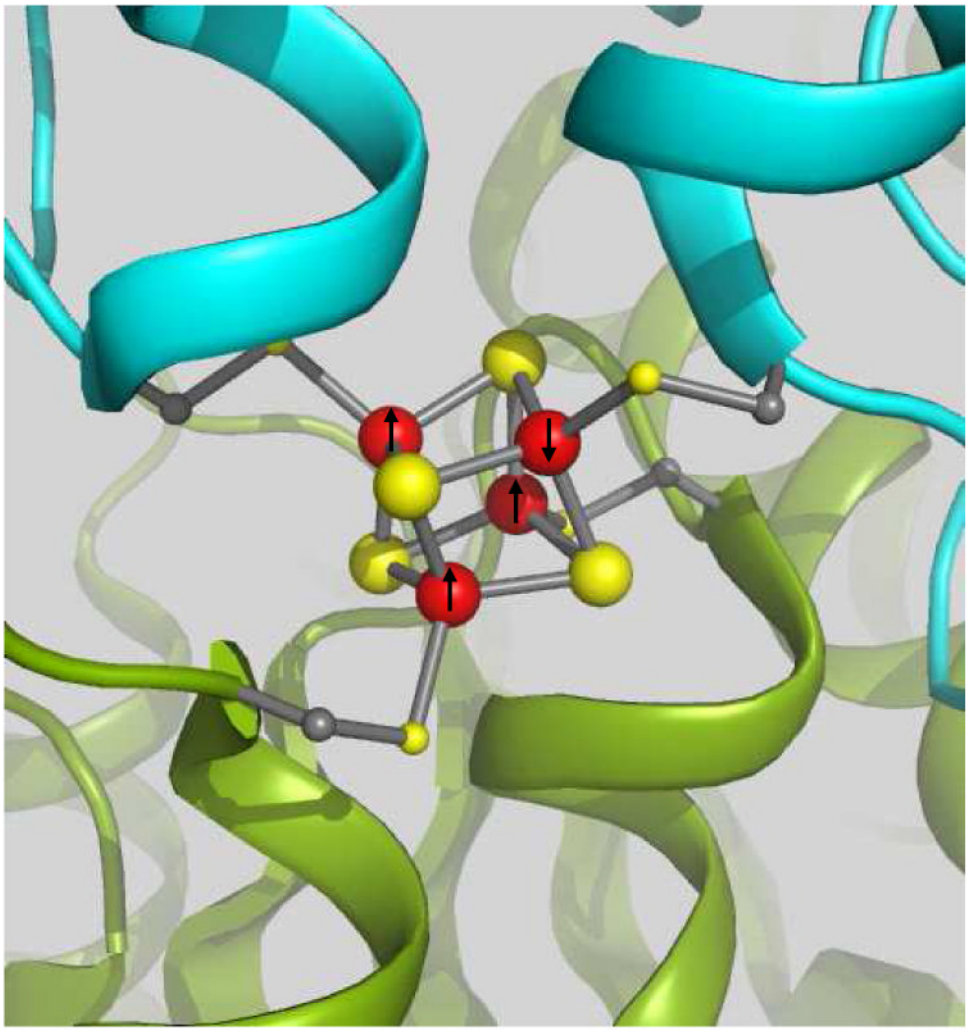

Figure 12.

Segment of the all-ferrous Fe-protein (PDB code 1G1M) viewed from the solvent exposed face of the $[Fe_4S_4]^0$ cluster. Color code: subunit A (blue ribbon), subunit B (green ribbon), irons (red spheres) and sulfurs (yellow spheres). The front iron atom connected to subunit A is labeled Fe(3) in the PDB file and Fe_4 in our discussion and is the iron site that has been identified as the unique spectroscopic site of the cluster in this work. The front iron atom connected to subunit B is labeled Fe(1) in the PDB file and Fe_1 in our discussion. The ordering of the iron spins in the $S = 4$ state of the all-ferrous cluster is indicated by arrows; the arrow at the unique site points downward; the arrows of the “equivalent” sites point upward.

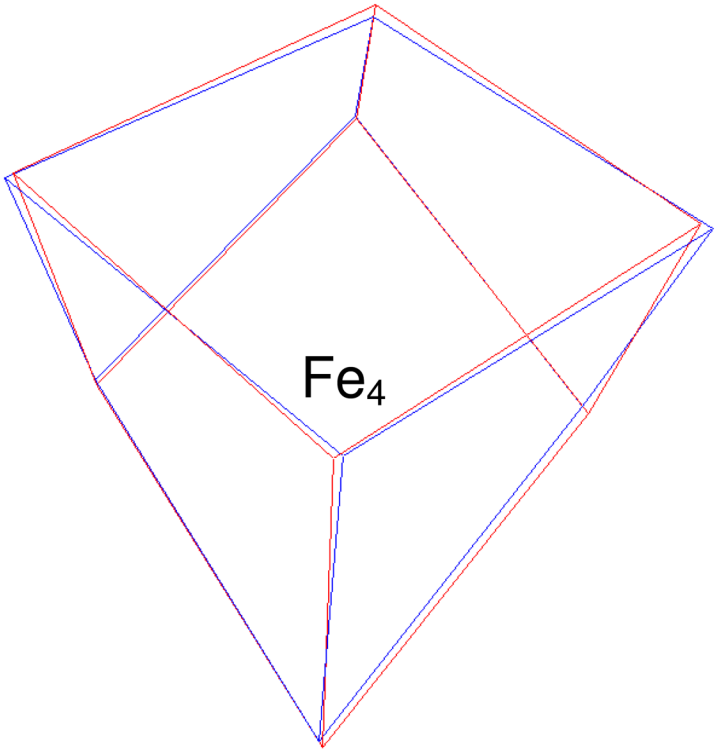

Figure 13.

Overlay of the all-ferrous Fe–S core in complex **1** (red) and the one in the Fe-protein of *A. vinelandii* (blue). The overlay is obtained by minimizing the RMSD between the corresponding iron and sulfur atoms of the two cores for the site-to-site mapping defined in case 1 of Table 8. Case 1 is one of the three mappings that map the unique sites (labeled Fe_4) of the two cores onto each other and give significantly lower RMSDs.

Table 1

Mössbauer parameters for the $S = 4$ state of complex **1**[a] and $[4Fe\text{-}4S]^0$ state of the *Av*2[b]

site[c]		δ[d] (mm/s)	ΔE_Q[d] (mm/s)	η	α_{efg} (°)	β_{efg} (°)	γ_{efg} (°)	A_x (KG)	A_y (KG)	A_z (KG)	α_A (°)	β_A (°)	γ_A (°)
1[e]	**1**	0.61	-1.6	0	0	90	0	-74	-65	-66.5	0	0	0
	*Av*2	0.68	-1.24	0.54	0	90	90	-98	-79	-70	0	0	0
2 & 3	**1**	0.62	-1.5	0.1	0	105	0	-98	-57	-70	0	15	0
2	*Av*2	0.68	-1.72	0	0	56.6	4.6	-86	-76	-81	0	0	0
3	*Av*2	0.68	-1.48	0	0	92.3	0	-100	-73	-73	0	0	0
4[e]	**1**	0.54	2.96	0.59	0	90	90	7.7	57	29	0	0	0
	*Av*2	0.68	3.08	0.59	90	90	52.8	22	25	63	0	150	0

[a] $D = -1.9$ cm^{-1} and $E/D = 0.07$ was used for the simulation.

[b] $D = -0.75$ cm^{-1} and $E/D = 0.33$ was used for the simulation.

[c] The Fe sites of the *Av*2 labeled 1, 2, 3 and 4 corresponds with the sites 4, 2, 3 and 1 in ref 6, respectively.

[d] At 4.2 K.

[e] For the site 1 and 4 of the *Av*2 the coordinate frame $\{x', y', z\}'$ was adopted to fulfill the convention $0 \leq \eta \leq 1$.

Table 2

Spin quantum numbers, numbers of spin multiplets, spin state energies, and relative energies for all-ferrous cluster with six equal exchange-coupling constants between the four irons

S	# multiplets	$E°(S)/J°$	$[E°(S) - E°(0)]/J°$
0	5	−12	0
1	12	−11	1
2	16	−9	3
3	17	−6	6
4	15	−2	10
5	10	3	15
6	6	9	21
7	3	16	28
8	1	24	36

Table 3

Subcluster spins in $S = 4$ states

S	S_{12}	S_{123}	# multiplets
4	0 – 4	2	5
4	1 – 4	3	4
4	2 – 4	4	3
4	3, 4	5	2
4	4	6	1

Table 4

Size and energy of T_2 distortion[a]

S	S_{123}^{max}	$12\,\kappa_T \delta J_T^{min}(S)$	$48\,\kappa_T\,\Delta E_T\,(S)/J°$
0	2	0	0
1	3	5	−50
2	4	11	−242
3	5	18	−648
4	6	26	−1352
5	6	21	−882
6	6	15	−450
7	6	8	−128
8	6	0	0

[a]The values listed for S_{123}^{max} follow from the triangular inequalities for the coupling of S_{123} ($0 \le S_{123} \le 6$) and S_4 to resultant spin S: $|S_{123} - S_4| \le S \le S_{123} + S_4$.

Table 5

Size and energy of E distortion

S	$12\,\kappa_E \delta J^E_{min}(S)$	$48\,\kappa_E\,\Delta E_E\,(S)/J°$
0	36	−1296
1	35	−1225
2	33	−1089
3	30	−900
4	26	−676
5	21	−441
6	15	−225
7	8	−64
8	0	0

Table 6

Condition $\kappa_T / \kappa_E < q_S$ for which T_2 minimum is below E minimum for given value of S

S		q_S
0	0	0.000 [a]
1	$^2/_{49}$	0.041 [b]
2	$^2/_9$	0.222
3	$^{18}/_{25}$	0.720
4 – 7	2	2.000
8	_ [c]	–

[a] E minimum is below T_2 minimum for any positive value of κ_E.

[b] Decimal representation of ratio.

[c] Jahn–Teller inactive in both T_2 and E spaces.

Table 7

Conditions $\kappa_T < p_S$ for which the T_2 minimum for $S = 4$ is lower in energy than the T_2 minimum for $S = 0$, 1, 2, and 3.

S	p_S	
0	$^{169}/_{60}$	2.817 [a]
1	$^{217}/_{72}$	3.014
2	$^{185}/_{56}$	3.304
3	$^{11}/_{3}$	3.666

[a] Decimal representation of ratio.

Table 8

Fe-S-Fe bond angles in all-ferrous clusters in *Av*2 and complex **1**

	$Fe_iS_kFe_j$ (°) [a,b]	
i, k, j	**protein**	**complex 1**
1,2,4	74.0	71.9
1,3,4	73.7	71.2
2,1,4	70.8	71.2
2,3,4	70.5	71.3
3,1,4	70.7	73.2
3,2,4	70.7	73.4
av.	**71.7**	**72.0**
1,3,2	66.8	68.0
1,4,2	66.9	67.3
1,2,3	69.9	69.8
1,4,3	68.5	70.0
2,1,3	65.7	68.0
2,4,3	64.5	67.5
av.	**67.1**	**68.4**

[a] The sulfur atoms carry the same labels as the diagonally opposite irons (Figure 8).

[b] The sites here labeled Fe_1, Fe_2, Fe_3, Fe_4 correspond with Fe(1), Fe(4), Fe(2), Fe(3) in the PDB file 1G1M containing the structure of the all-ferrous Fe-protein of *A. vinelandii* and with Fe(1), Fe(3), Fe(4), Fe(2) of complex **1** in the labeling of ref 2, respectively.

Table 9

Root mean squares deviations for the twelve overlays of the all-ferrous clusters in *Av*2 and complex **1**

Case	Mapping	RMSD 4Fe (Å)	RMSD 4Fe-4S (Å)
1	1,2,3,4 [a]	**0.053**	**0.060**
2	2,3,1,4	**0.071**	**0.070**
3	3,1,2,4	**0.050**	**0.066**
4	2,4,3,1	0.121	0.127
5	4,1,3,2	0.099	0.096
6	3,2,4,1	0.095	0.094
7	4,2,1,3	0.068	0.081
8	1,3,4,2	0.121	0.127
9	1,4,2,3	0.103	0.102
10	3,4,1,2	0.122	0.122
11	4,3,2,1	0.089	0.090
12	2,1,4,3	0.102	0.105

[a] Mapping of iron sites in all-ferrous cluster in nitrogenase to those of the all-ferrous cluster in complex **1**. For example, in case 2: $Fe_1 \rightarrow Fe_2$, $Fe_2 \rightarrow Fe_3$, $Fe_3 \rightarrow Fe_1$, $Fe_4 \rightarrow Fe_4$ (nitrogenase → complex **1**).